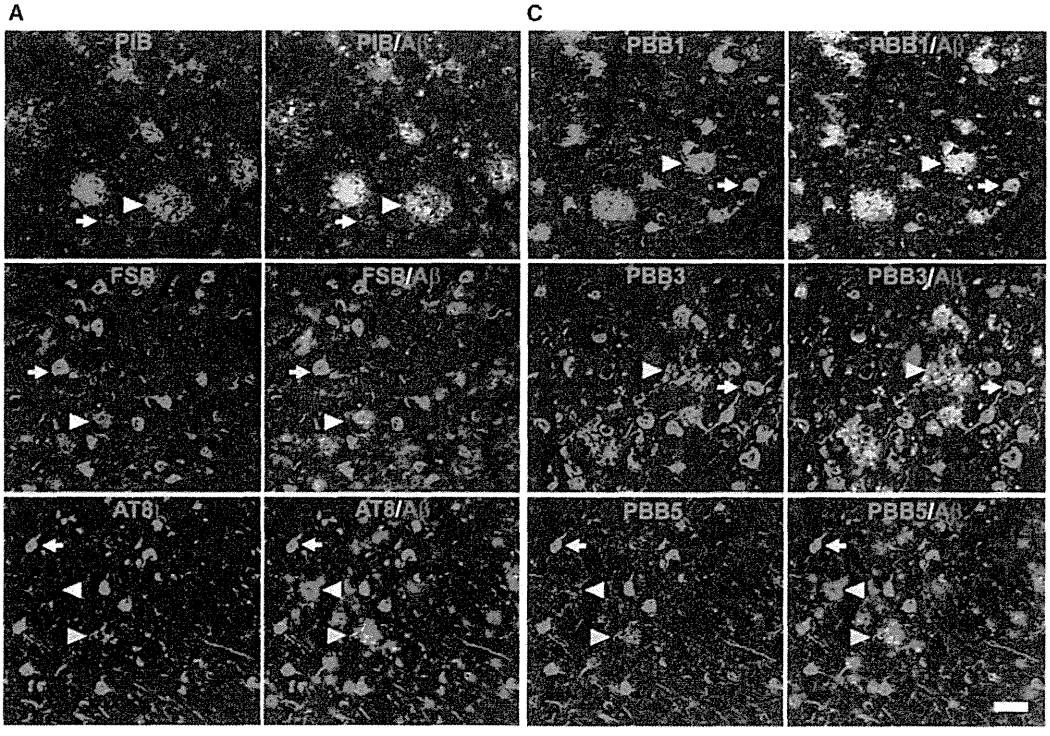

B

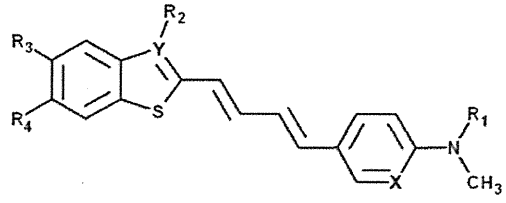

Compound	R_1	R_2	R_3	R_4	X	Y	ClogP
PBB1	CH_3	-	H	H	C(H)	N	5.44
PBB2	H	-	H	OH	C(H)	N	3.57
PBB3	H	-	H	OH	N	N	3.30
PBB4	H	-	OH	OH	C(H)	N	2.97
PBB5	CH_3	CH_3CH_2	H	H	C(H)	N^+	2.32

Figure 1. Design and Characterization of PBB Compounds as Potential Imaging Agents for Tauopathies

(A) Confocal fluorescence images of frontal cortex sections from an AD patient. Following fluorescence labeling (pseudocolors are converted to green) with PIB (top row) and FSB (middle row), the samples were immunostained with an antibody against AβN3(pE) (red in the right column). PIB intensely labeled Aβ plaques (white arrowheads) but did not clearly label NFTs (arrows). By contrast, NFTs and neuropil threads were intensely labeled by FSB, whereas the staining of diffuse plaques was negligible. A section was also doubly immunolabeled (bottom row) with AT8 (green) and anti-AβN3(pE) antibodies (red in the right panel), to demonstrate the abundance of tau and Aβ amyloids in this area. Yellow arrowheads indicate tau-positive dystrophic neurites associated with senile plaques.

(B) Structures of PBBs. Neutral benzothiazoles (PBB1-4) are newly synthesized chemicals, and a charged benzothiazolium, PBB5, is identical to a commercially available near-infrared laser dye.

(C) Confocal fluorescence images of PBBs (pseudocolors are converted to green) and AβN3(pE) (red in the right column) staining in sections adjacent to those displayed in (A). The intensity of plaque staining (arrowheads) relative to that of NFTs (arrows) was positively associated with the lipophilicity of PBBs. As compared with PBB1 (top row) staining, labeling of diffuse plaques with PBB3 (middle row) was substantially attenuated. PBB5 was nearly unreactive with diffuse plaques (bottom row), and subsequent double immunofluorescence staining of the same section (bottom row in C) illustrated good agreement of PBB5 labeling with the distribution of AT8-positive NFTs.

Scale bar, 50 μm (A and C). See also Figure S1 and Table S1.

staining with thioflavin-S, FSB, and AT8 (Figure 3B). On the other hand, no overt in vitro (Figure 3A) or ex vivo (data not shown) fluorescence of these ligands was noted in the corresponding regions of non-Tg wild-type (WT) mice. Consistent with these observations, two-photon laser scanning fluorescence microscopy of ex vivo samples demonstrated somatic and neuritic staining of a subset of tangle-bearing neurons with intravenously injected 2-[4-(4-methylaminophenyl)-1,3-butadienyl]-benzothiazol-6-ol (PBB2) and PBB4 in unsliced spinal cord blocks from PS19 mice (Figure 3B).

In Vivo Macroscopic and Mesoscopic Optical Detection of Fibrillar Tau Pathologies in a Mouse Model Using PBB5

We next characterized PBBs with the use of in vivo fluorescence imaging modalities, which permitted a quick assessment of

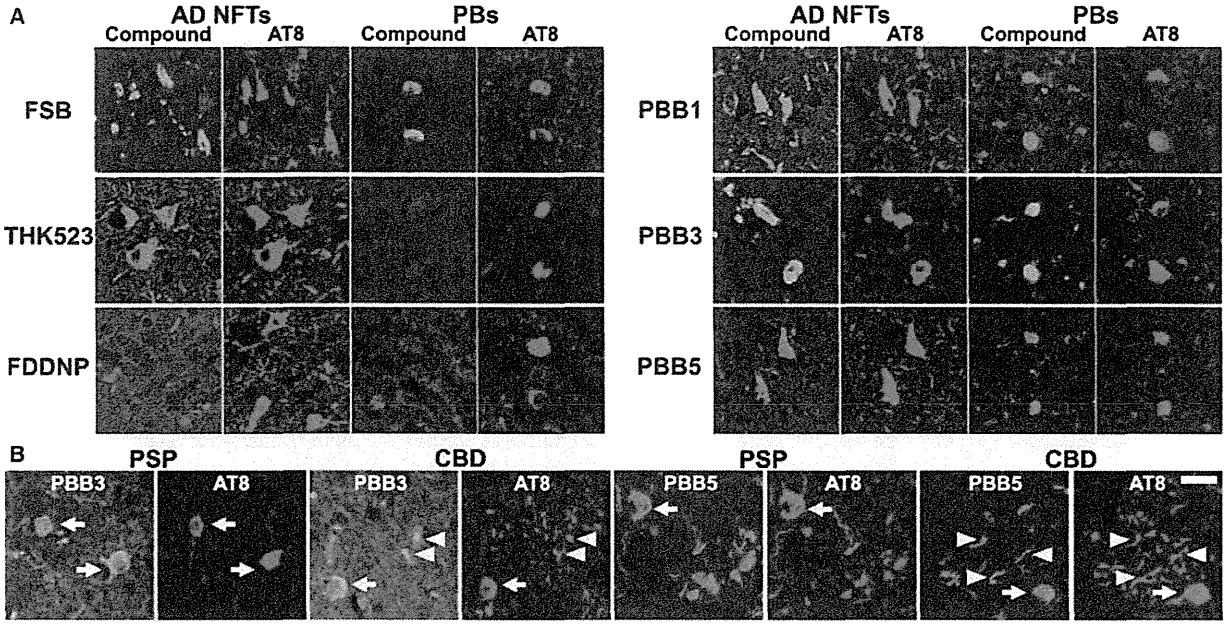

Figure 2. Binding of Tau Ligands to Tau Lesions in AD and Non-AD Tauopathy Brains

(A) Double fluorescence staining of AD NFTs and Pick bodies (PBs) in Pick's disease with PBBs, other tau ligands, and anti-phospho-tau antibody (AT8). FSB and PBBs sensitively captured AD NFTs and PBs. AD NFTs were labeled with THK523. Meanwhile, PBs were not visualized by these compounds. NFTs and PBs were barely recognizable by using FDDNP.

(B) Double fluorescence staining of neuronal tau inclusions (arrows) in PSP and CBD and putative astrocytic plaques (arrowheads) in CBD. A substantial portion of tau fibrils in neurons were captured by PBB3 and PBB5, but a much smaller subset of phosphorylated tau aggregates in astrocytic plaques were labeled with these compounds.

Scale bar, 20 μm (A and B). See also Figures S2 and S3.

candidate chemicals without the need for radiolabeling. Because PBB5 is fluorescent, with peak excitation and emission wavelengths in a near-infrared range (Table S1), this compound is applicable to in vivo optical imaging of tau deposits in laboratory animals. To examine this possibility, fluorescence images were obtained from living mice over a time course following intravenous PBB5 injections using a small animal-dedicated system permitting the intravital observation of fluorescence signals at magnifications varying between macroscopic and microscopic levels. Tail vein administration of PBB5 in PS19 mice revealed strong fluorescence relative to non-Tg WT mice in the central nervous system (CNS) above the slit between the base of the skull and first vertebra, through the skin and connective tissues overlaying the cisterna magna (Figures S3A–S3D), suggesting a concentration of this tracer in the PS19 spinal cord. In line with this in vivo observation, the hindbrain and spinal cord of PS19 mice, which were dissected out at 2 hr after the injection of PBB5, exhibited increased retention of this compound compared to non-Tg WT mice (Figures S3E–S3G).

In vivo optical imaging of tau Tg mice was subsequently performed using a device equipped with a pulsed diode laser and a photomultiplier tube to detect deep signals through the skull. Elevated levels of fluorescence intensity were found in homogenized brain stem samples collected from PS19 mice at 20 hr after the intravenous tracer administration (Figure S4A), indicating a long-lasting in vivo binding of PBB5 to tau fibrils. To support the ex vivo evidence, fluorescence intensity was noninvasively analyzed in living PS19 and non-Tg WT mice treated with PBB5. The mice, with their heads shaved in advance, were prescanned, and autofluorescence signals were detected at a relatively high level in an area corresponding to the frontal forebrain. Using these baseline signals as landmarks, regions of interest (ROIs) were defined in the frontal cortex, brain stem, and spinal cord (Figure 4A). The near-infrared fluorescence was notably increased immediately after the intravenous injection of PBB5 (Figure S4C), and the fluorescence in the brain stem and spinal cord ROIs of PS19 mice much exceeded that in WT mice at 30 min (Figure 4B). Fluorescence intensity in the frontal cortex ROI, normalized on the basis of integration time and laser power, was lower in PS19 mice than in WT mice over 120 min after tracer injection (Figure S4B), which may reflect impaired CNS delivery of the tracer in Tg mice due to degenerative changes (see Figures S4C–S4L for details), and thereafter this became almost equivalent between the two genotypes (Figure S4B). Meanwhile, persistent retention of the signals in the brain stem and spinal cord ROIs of PS19 mice was observed beyond 240 min (Figures 4B and S4B). A more quantitative index comparable among different mice was determined by calculating the target-to-frontal-cortex ratio of fluorescence intensity and was shown to increase over time particularly in PS19 mice (Figures 4C and 4D). This ratio was significantly greater in PS19 mice than in WT mice at 240 min (Figure 4E), beyond which the difference

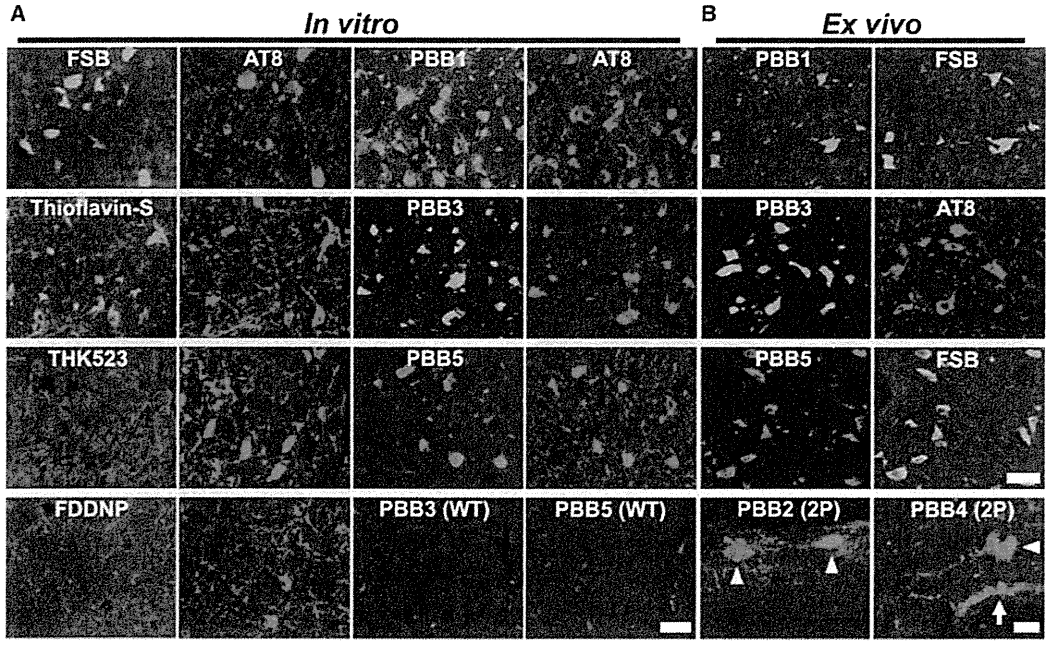

Figure 3. In Vitro and Ex Vivo Labeling of NFTs in PS19 Mice with PBB Compounds

(A) Double fluorescence staining of intraneuronal tau aggregates in postmortem brain stem slices of a 12-month-old PS19 mouse with PBB, other amyloid ligands, and anti-phospho-tau antibody (AT8).

(B) Binding of intravenously administered PBBs (0.1 mg/kg PBB5 and 1 mg/kg PBB1 and PBB3) to NFTs in PS19 mice at 10–12 months of age. The tissues were sampled at 60 min after tracer administration. The brain stem (top row) and spinal cord (second and third rows from the top) sections abundantly contained neurons showing strong fluorescence (left), and subsequent staining with FSB or AT8 (right) indicated that these cells were laden with tau amyloid fibrils (right). Putative intraneuronal tau inclusions in unsectioned spinal cords (arrowheads in the bottom row) removed from PS19 mice at 60 min after intravenous injection of PBB2 and PBB4 were also clearly visible by using a two-photon (2P) fluorescence microscopic system. Arrow in the bottom row indicates a cluster of autofluorescence signals from blood cells.

Scale bars, 25 μm (A), 30 μm (top to third rows in B), and 20 μm (bottom row in B).

between the two lines of mice became nearly constant (Figures 4C and 4D). The intensity ratio of the spinal cord ROI to the frontal cortex in PS19 mice at 240 min was also significantly correlated with the abundance of NFTs stained with FSB (Figure 4F), but such correlations were not statistically significant in the brain stem (Figure 4F), implying limitations of the intensitometry in some brain regions below the cerebellum and fourth ventricle.

Intravital Imaging of Individual Tau Inclusions by PBB3 and Two-Photon Laser Scanning Fluorescence Microscopy

Two-photon excitation microscopy, which enables optical sectioning, potentially up to 1 mm deep, in living tissues, could be utilized to visually demonstrate transfer of a fluorescent probe from the plasma compartment into the cytoplasm of CNS neurons and binding of the probe to intraneuronal tau inclusions. We therefore captured fluorescence signals from intravenously administered PBB3 by in vivo two-photon laser scanning microscopic imaging of the spinal cord of laminectomized PS19 mice. Within 3 s of PBB3 injection, green fluorescence signals emerged in blood vessels prelabeled with red with intraperitoneal treatment using sulforhodamine 101 and subsequently diffused from the vasculatures to the spinal cord parenchyma over the next few minutes (Figures 5A–5F). These diffuse signals declined thereafter due to the clearance of PBB3 from the tissue, whereas intense labeling of putative tau inclusions with green fluorescence appeared in a subpopulation of large cells morphologically identified as neurons at 3–5 min after PBB3 injection (Figures 5G and 5H). These intracellular PBB3 fluorescent signals were not found in the spinal cord of WT mice (Figure 5I). As the BBB of the brain and spinal cord are presumed to be identical, the two-photon microscopic data obtained here provide compelling evidence that PBB3 rapidly transits the BBB and neuronal plasma membranes, where it binds to intraneuronal tau inclusions. Accumulation of injected PBB3 in AT8-positive, NFT-like lesions of Tg mice was postmortemly confirmed by ex vivo microscopy (Figures 5J and 5K).

Autoradiographic and PET Imaging of Tau Lesions in PS19 Mice by Radiolabeled PBBs

We investigated the kinetic properties of PBBs by high-performance liquid chromatography (HPLC) analyses of plasma and brain samples collected from non-Tg WT mice treated with these ligands. Following intravenous administration, PBB5 was rapidly converted into a major metabolite, which at 5 min was found at high levels in both plasma and brain extracts. Subsequent liquid

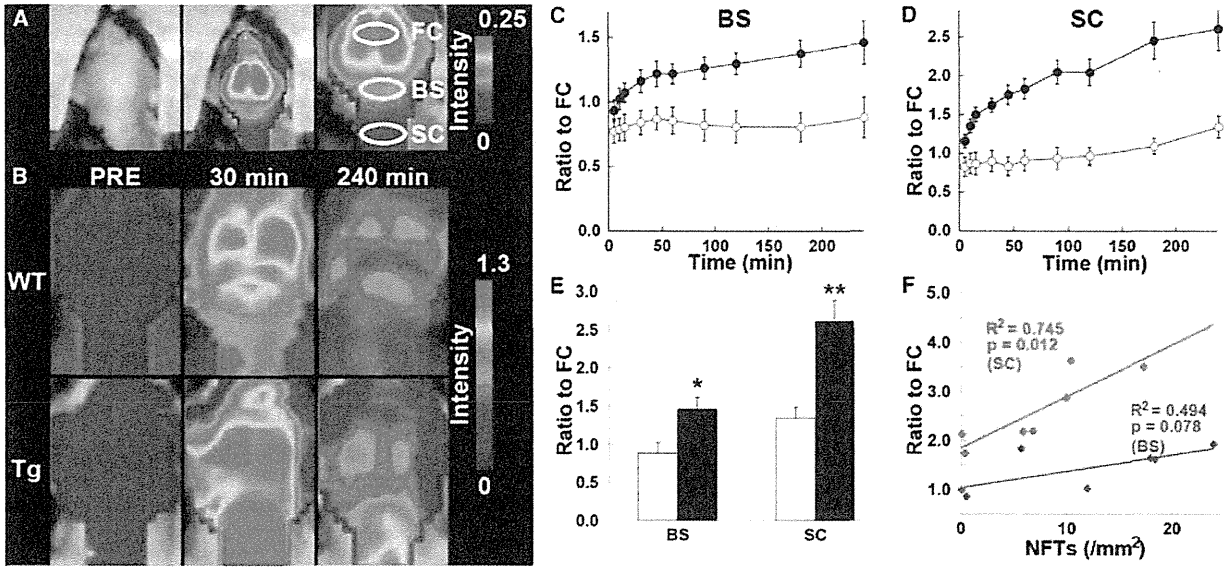

Figure 4. Noninvasive Near-Infrared Imaging of Tau Pathology in Living Tau Tg Mice Using Pulsed Laser Optics and PBB5

(A) Baseline autofluorescence signals (middle) are overlaid on the visible background image of a shaven non-Tg WT mouse head (left). Ellipsoidal ROIs are defined above the frontal cortex (FC), brain stem (BS), and cervical spinal cord (SC) guided by a relatively intense emission from the FC region (right).

(B) Fluorescence intensity maps in 12-month-old WT (top) and PS19 (Tg; bottom) mice before and at 30 and 240 min after the intravenous administration of PBB5 (0.1 mg/kg). The intensity maps (A and B) are normalized by the FC ROI value at 30 min after tracer injection. Long-lasting retention of the tracer was noted in the BS and SC ROIs of the Tg mouse.

(C and D) Target-to-FC ratios of fluorescence intensity in the BS (C) and SC (D) ROIs over the image acquisition time in the WT (open circles; n = 7) and PS19 (closed circles; n = 7) mice. There were significant main effects of time, region, and genotype in two-way, repeated-measures ANOVA (time, $F_{(11, 132)} = 17.6$, $p < 0.001$; region, $F_{(1, 12)} = 29.9$, $p < 0.001$; genotype, $F_{(1, 12)} = 23.6$, $p < 0.001$).

(E) Target-to-FC ratios in the BS and SC ROIs of the WT (open columns) and tau Tg (closed columns) mice at 240 min after tracer injection. $^*p < 0.05$; $^{**}p < 0.01$; two-way repeated-measures ANOVA with Bonferroni's post hoc analysis.

(F) Scatterplots of target-to-FC ratios at 240 min versus the number of FSB-positive NFTs per unit area of postmortem 20 μm tissue slices in BS (blue symbols) and SC (red symbols) ROIs of tau Tg mice. Solid lines represent regressions; p values were determined by t test. Vertical bars in the graphs represent SEs.

See also Figures S3 and S4.

chromatography-mass spectrometry (LC-MS) assays suggested that the major metabolite was likely a reduced, electrically neutralized derivative of PBB5 (Figures S5A and S5B). Besides transventricular uptake of unmetabolized PBB5 as implied above, this uncharged form incapable of emitting near-infrared light could readily penetrate the BBB, as well as cell membranes, and thereafter could be reoxidized into its original form, thereby enabling it to bind to tau fibrils, particularly at sites exposed to oxidative stress in pathological conditions. In addition, PBB4 was promptly converted to metabolites capable of entering the brain. Finally, studies of PBB2 and PBB3 showed that they exhibited reasonable biostability and sufficient entry into and clearance from the brain. Indeed, HPLC assays demonstrated that fractions of unmetabolized PBB2 and PBB3 in mouse plasma were 23.5% and 16.3%, respectively, at 3 min after intravenous administration and were 4.6% and 2.8%, respectively, at 30 min. There were also no metabolites of PBB2 and PBB3 detectable in the mouse brain at 3 and 30 min.

We then radiolabeled PBB2 and PBB3 with ^{11}C to conduct autoradiographic and PET assays using PS19 mice. In vitro autoradiography using frozen tissue sections showed binding of these radioligands to the brain stem of PS19 mice and neocortex of AD patients (Figure 6A). As expected from their lipophilicities, [^{11}C]PBB3 yielded high-contrast signals with less nonspecific labeling of myelin-rich white matter than did [^{11}C]PBB2, and the accumulation of [^{11}C]PBB3 in pathological regions was nearly completely abolished by the addition of nonradioactive compounds. Similarly, ex vivo autoradiographic studies demonstrated that intravenously administered [^{11}C]PBB3 selectively labeled the brain stem and spinal cord of PS19 mice harboring neuronal tau inclusions, whereas tau-associated [^{11}C]PBB2 radiosignals were less overt because of a considerable level of nonspecific background (Figure 6B; Figures S6C–S6F). Finally, in vivo visualization of tau lesions in PS19 mouse brains was enabled by a microPET system using these two tracers (Figures 6C, S6A, and S6B). Following intravenous injection, [^{11}C]PBB3 rapidly crossed the BBB and unbound and nonspecifically bound tracers were promptly washed out from the brain with a half-life of ~10 min (left panel in Figure 6E). The retention of [^{11}C]PBB3 signals in the brain stem of 12-month-old PS19 mice lasted over the imaging time (90 min), producing a pronounced difference from that in age-matched non-Tg WT mice (left panel in Figure 6E). By selecting the striatum as a reference region lacking tau deposits, the target-to-reference ratio was estimated for the brain stem, with the value in PS19 mice peaking at around 70 min, contrasting with its continuous decrease over

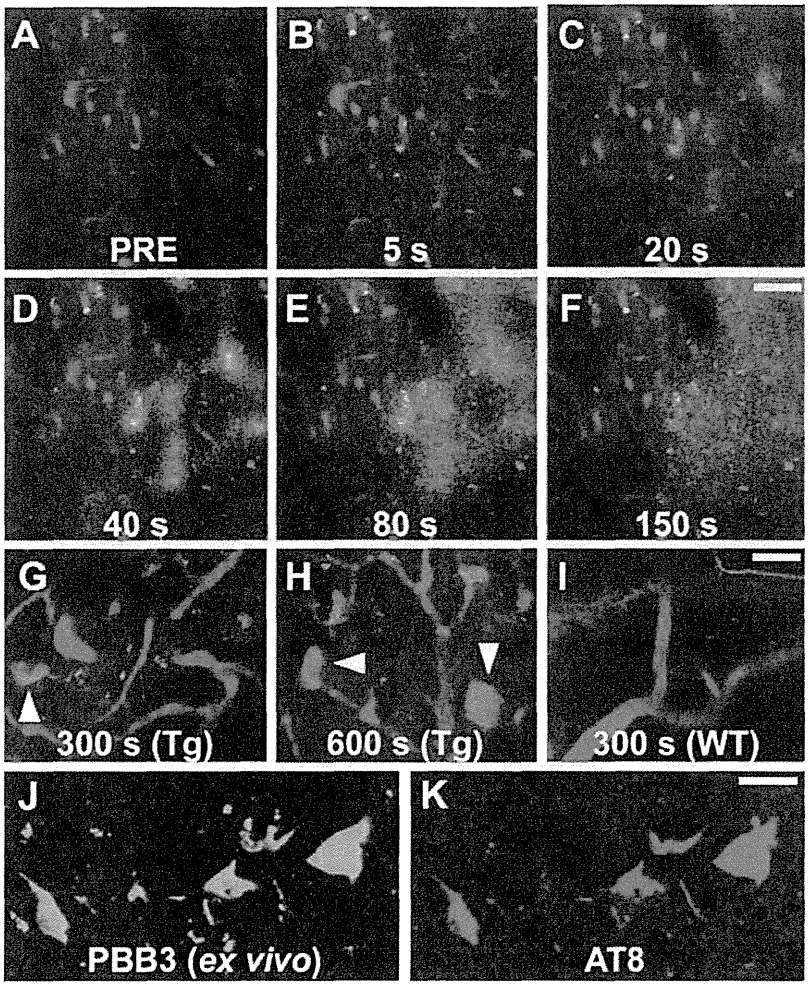

Figure 5. Real-Time Two-Photon Laser Scanning Images of PBB3 Diffusing from Vessels, Binding to Intraneuronal Tau Inclusions, and Clearing from Spinal Cord

(A–H) A maximum projection of fluorescence in a 3D volume of the spinal cord of a living PS19 mouse at 12 months of age before (A) and at various time points after (B–H) intravenous administration of PBB3 (1 mg/kg). Blood vessels were labeled with sulforhodamine 101 (red) intraperitoneally injected at 15 min before PBB3 administration. Green fluorescence indicates a rapid transfer of PBB3 from the plasma to tissue parenchyma (B–E) and subsequent washout from the tissue (F). Background PBB3 signals were further attenuated beyond 300 s, whereas somatodendritic labeling by this compound was observed in a subset of neurons (arrowheads in G and H).

(I) Fluorescence image of WT spinal cord at 300 s after PBB3 injection demonstrates no overt retention of the tracer in the tissue.

(J and K) Ex vivo microscopy for a brain stem section of the same Tg mouse. Tissues were obtained at 60 min after PBB3 injection. Signals of intravenously administered PBB3 (J) overlapped with AT8 immunoreactivity (K).

Scale bars, 50 μm (A–F), 25 μm (G–I), and 25 μm (J and K).

60 min in WT mice (right panel in Figure 6E). The mean ratio at 45–90 min was increased by 40% in 12-month-old PS19 mice as compared with age-matched WT mice ($p < 0.01$ by t test). The agreement between localizations of PET signals and tau inclusions in PS19 mice was proven by postmortem FSB staining of brain sections from scanned mice (Figure 6D). Significantly, the mean target-to-reference ratio in the brain stem quantified by PET correlated closely with the number of FSB-positive inclusions per brain section in the same region of the postmortem sample ($p < 0.001$ by t test; data not shown). [^{11}C]PBB2 exhibited slower clearance from the brain and higher nonspecific retention in myelin-rich regions than [^{11}C]PBB3 (Figure S6G), resulting in insufficient contrast of tau-bound tracers in the brain stem of PS19 mice and a small difference in the target-to-reference ratio of radioactivities between PS19 and WT mice (8% at 45–90 min; $p < 0.05$ by t test; Figure S6H) relative to those achieved with [^{11}C]PBB3.

As radiolabeling at the dimethylamino group in PBB5 with ^{11}C was unsuccessful, ^{11}C-methylation of a hydroxyl derivative of this compound was performed, leading to the production of [^{11}C]methoxy-PBB5 ([^{11}C]mPBB5; Figure S5C). PET images demonstrated complex pharmacokinetics of [^{11}C]mPBB5 (Figures S5D and S5E), and the difference in the specific radioligand binding between Tg and WT mice was small relative to the [^{11}C]PBB3-PET data (Figure S5F). After taking all of these findings into consideration, [^{11}C]PBB3 was selected as the most suitable ligand for in vivo PET imaging of tau pathology in tau Tg nice and human subjects.

Notably, the hippocampus of many PS19 mice was devoid of overt [^{11}C]PBB3 retention (Figure 6C), although a pronounced hippocampal atrophy was noted in these animals. This finding is in agreement with the well-known neuropathological features of PS19 mice in the hippocampus, because the accumulation of AT8-positive phosphorylated tau inclusions results in the degeneration of the affected hippocampal neurons prior to or immediately after NFT formation, followed by the clearance of their preNFTs or NFTs that are externalized into the interstitial CNS compartment (Figure S2). To explore the feasibility of our imaging agents in studies with other tauopathy model mice, we also performed fluorescence labeling with PBBs for brain sections generated from rTg4510 mice (Santacruz et al., 2005; the Supplemental Experimental Procedures). As reported elsewhere (Santacruz et al., 2005), these mice developed numerous thioflavin-S-positive neuronal tau inclusions in the neocortex and hippocampus, and reactivity of these lesions with PBBs was demonstrated by in vitro and ex vivo fluorescence imaging (Figure S7).

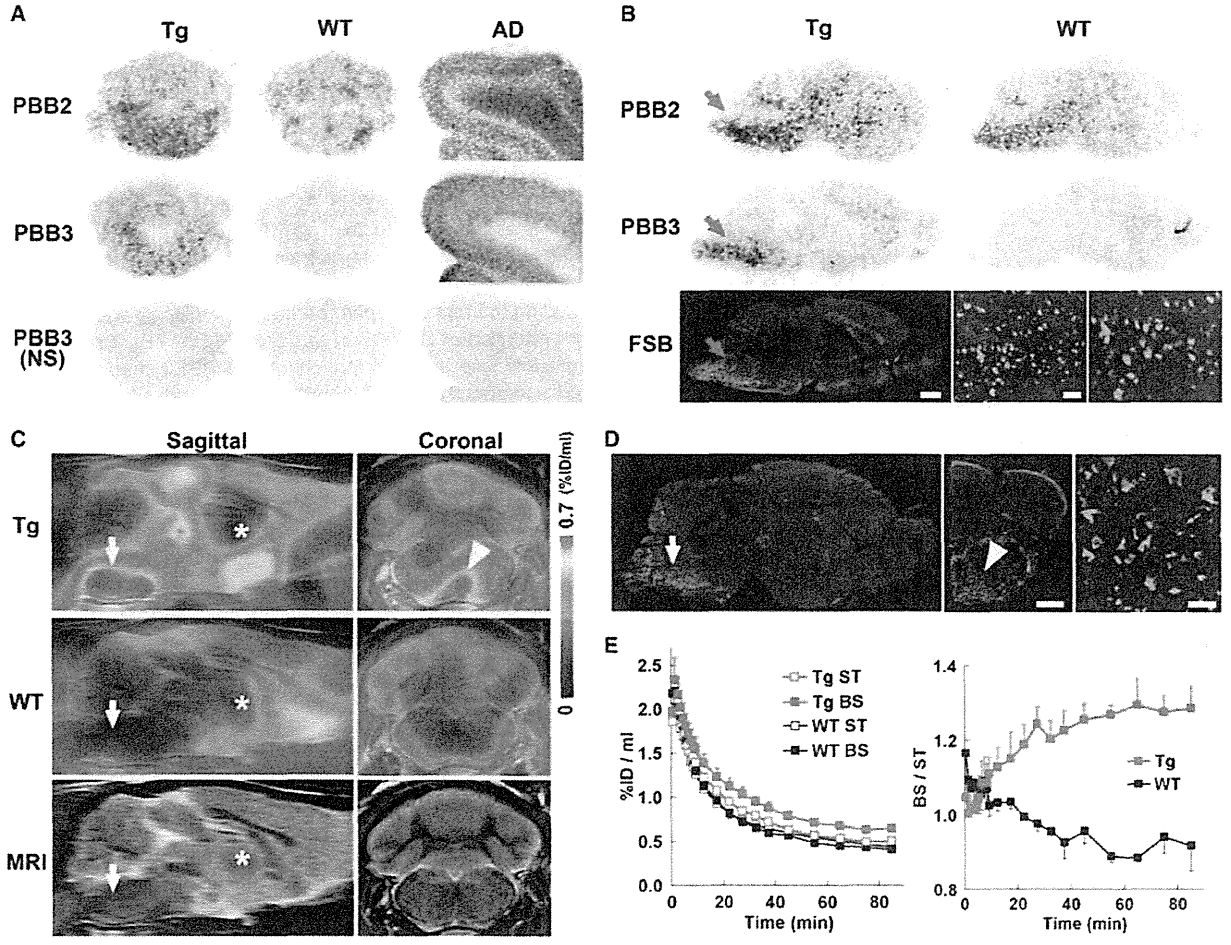

Figure 6. PET and Autoradiographic Detection of Tau Pathologies in PS19 Mice Using [^{11}C]PBB2 and [^{11}C]PBB3

(A) In vitro autoradiograms of PS19 and non-Tg WT hindbrains (coronal sections) and AD frontal cortex. Fibrillar aggregates in the mouse brain stem and AD gray matter produced intense radiolabeling with both tracers, but nonspecific background signals were also observed at a considerably high level with the use of [^{11}C]PBB2. Binding of [^{11}C]PBB3 was profoundly abolished by the addition of nonradioactive PBB3 (10 μM).

(B) Autoradiographic labeling with intravenously injected [^{11}C]PBB2 and [^{11}C]PBB3 in PS19 (Tg) and WT mice. The brains were removed at 45 min after injection and were cut into sagittal slices. The autoradiographic section of PS19 brain was also stained with FSB. Arrows indicate the brain stem containing numerous tau inclusions displayed at intermediate and high magnifications.

(C) Sagittal and coronal PET images generated by averaging dynamic scan data at 60–90 min after intravenous administration of [^{11}C]PBB3. The images are overlaid on the MRI template (images of the template alone are presented at the bottom). Arrows and asterisks indicate the brain stem and striatum, respectively, and arrowhead denotes intense radiolabeling in the medial brain stem of the PS19 mouse.

(D) FSB staining of PS19 mouse brain shown in (C). Sagittal (left) and coronal (middle) images and a high-power view of fibrillar inclusions (right) are displayed. Corresponding to high-level retention of [^{11}C]PBB3 in PET scans, abundant FSB-positive lesions were found in the medial brain stem (arrow and arrowhead).

(E) Time-radioactivity curves (left) in the striatum (ST) and brain stem (BS) and BS-to-ST ratio of radioactivity (right) over the imaging time in PS19 (Tg; red symbols) and WT (black symbols) mice (n = 5 each). Vertical bars in the graphs denote SEs.

Scale bars, 1 cm (A and B, top, middle, and bottom left panels); 1 cm (C and D, left and middle panels); 100 μm (B, bottom middle panel); and 100 μm (B, bottom right panel and D, right panel). See also Figures S5, S6, and S7.

Detection of Tau Pathologies in Living Brains of AD Patients by Comparative PET Imaging with [^{11}C]PBB3 and [^{11}C]PIB

In order to compare the bindings of [^{11}C]PBB3 and [^{11}C]PIB to tau-rich regions in the human brain, in vitro autoradiography was carried out with sections of AD and control hippocampus. A notable difference in labeling between these two radioligands was observed in the CA1 sector and subiculum of the AD hippocampus, where fibrillar tau aggregates predominantly localized to NFTs and neuropil threads (Figure 7A).

We subsequently conducted an exploratory clinical PET study for patients with probable AD (n = 3) and age-matched cognitively normal control (NC) subjects (n = 3). All AD patients exhibited a marked increase in the retention of [^{11}C]PIB in

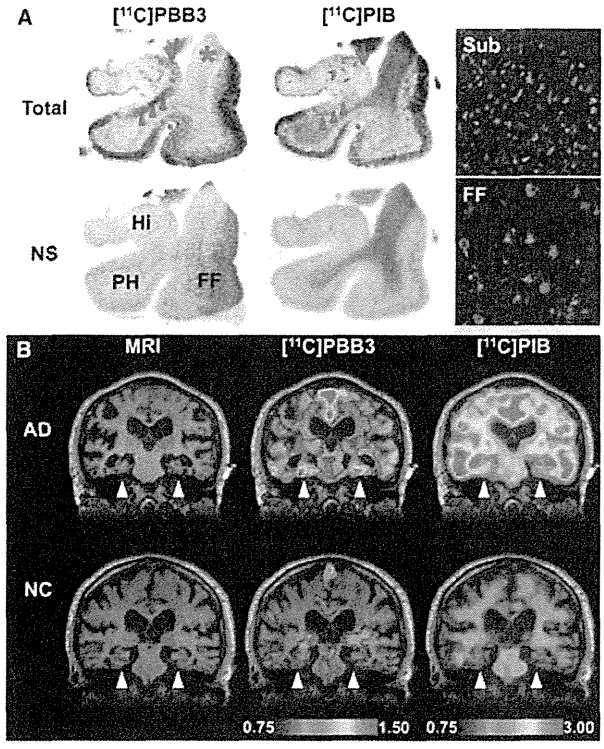

Figure 7. Accumulation of [^{11}C]PBB3 in the Hippocampal Formation of AD Patients Revealed by In Vitro Autoradiography and In Vivo PET

(A) Autoradiographic labeling of adjacent brain sections from an AD patient with 10 nM of [^{11}C]PBB3 (left) and [^{11}C]PIB (middle). The slices contain the hippocampus (Hi), parahippocampal gyrus (PH), fusiform gyrus (FF), and white matter (asterisks). Total binding (top) of [^{11}C]PBB3 and [^{11}C]PIB was markedly abolished (bottom) by addition of nonradioactive PBB5 (100 μM) and thioflavin-S (10 μM), respectively, except for the nonspecific (NS) labeling of white matter with [^{11}C]PIB. The hippocampal CA1 sector and subiculum displayed intense [^{11}C]PBB3 signals without noticeable binding of [^{11}C]PIB, and binding of [^{11}C]PBB3 in cortical areas flanking the collateral sulcus (identified by a red dot) and hippocampal CA2 sector (arrows) was also abundant relative to that of [^{11}C]PIB. FSB staining of amyloid fibrils in the sections used for autoradiography indicated the predominance of NFTs and diffuse plaques in the hippocampal subiculum (Sub) and fusiform gyrus (FF), respectively (right panels), supporting the strong reactivity of [^{11}C]PBB3 with AD NFTs.

(B) MRI (left) and PET imaging with [^{11}C]PBB3 (middle) and [^{11}C]PIB (right) performed in the same AD (top) and normal control (NC; bottom) subjects. Coronal images containing the hippocampal formation (arrowheads) are displayed. [^{11}C]PBB3- and [^{11}C]PIB-PET images were generated by estimating SUVRs at 30–70 min and 50–70 min after radiotracer injection, respectively, and were superimposed on individual MRI data. In the hippocampal formation, prominently increased retention of [^{11}C]PBB3 in the AD patient was in sharp contrast to the modest or negligible changes in [^{11}C]PIB binding as compared with NC. Scale ranges for SUVRs were 0.75–1.50 ([^{11}C]PBB3) and 0.75–3.00 ([^{11}C]PIB).

See also Figure S9.

plaque-rich areas, and all NC were negative for this PET assay. These subjects then received a [^{11}C]PBB3-PET scan, and the [^{11}C]PIB and [^{11}C]PBB3 images were compared in the same individuals. Intravenously injected [^{11}C]PBB3 was delivered to the brain tissue despite its relatively rapid metabolism in humans (Figures 9A and 9B). Unlike [^{11}C]PIB, [^{11}C]PBB3 showed minimal nonspecific binding to white matter and other anatomical structures with high myelin content, although it accumulated in dural venous sinuses in control and AD brains (Figures 7B, 8, and 9B). Time courses of regional radioactivity (Figures 9C and 9D; Figures S8A and S8B) and the standardized uptake value ratio (SUVR) to the cerebellum (Figures S8C and S8D) demonstrated accumulation of [^{11}C]PBB3 in several brain regions of AD patients as compared to controls (definition of these VOIs is indicated in Figure S8E). In agreement with autoradiographic findings, binding of [^{11}C]PBB3 to the medial temporal region, including the hippocampus, contrasted strikingly with the low-level retention of [^{11}C]PIB in this area (Figure 7B). There was a slight increase in the retention of [^{11}C]PBB3 primarily in the medial temporal region of a control subject with a loss of several points in Mini-Mental State Examination (MMSE) (subject 3 in Figure 8), appearing similar to the tau pathology at Braak stage III/IV or earlier (Braak and Braak, 1991), distinct from the lack of enhanced [^{11}C]PIB signals. Indeed, mild increase of medial temporal SUVR (Figure 9E) contrasted with unremarkable change in lateral temporal and frontal SUVRs in this subject (Figures 9G and 9H). Signals of [^{11}C]PBB3 were also intense mainly in the limbic region of a subject with early AD (subject 4 in Figure 8), but profound and moderate increases of SUVRs were also observed in the lateral temporal and frontal cortices, respectively, of this case (Figures 9G and 9H), resembling the localization of tau deposits at Braak stage V/VI (Braak and Braak, 1991). With the further cognitive decline as scored by MMSE (subjects 5 and 6 in Figure 8), additional increase in the retention of [^{11}C]PBB3 was found in the medial temporal region, precuneus, and frontal cortex (Figures 9E, 9F, and 9H). Meanwhile, a substantial decline of [^{11}C]PBB3 binding was noted in the lateral temporal cortex of subject 6 (Figures 8 and 9G). The SUVRs in the medial temporal region, precuneus, and frontal cortex were consequently well correlated with the decline of MMSE scores (Figures 9E, 9F, and 9H). In distinction with [^{11}C]PBB3-PET data, there was no overt association between the binding of [^{11}C]PIB and disease severity in AD patients (Figure 8), consistent with previous observations. These data support the potential utility of [^{11}C]PBB3 for clarifying correlations between the distribution of tau deposition and the symptomatic progression of AD.

As in vitro fluorescence staining indicated that PBB3 was reactive with not only tau lesions but also several types of senile plaques, particularly dense core plaques, density of binding sites, and affinity of [^{11}C]PBB3 for these sites were quantified by autoradiographic binding assays with hippocampal and neocortical sections of AD brains enriched with NFTs and senile plaques, respectively. These analyses demonstrated that specific radioligand binding sites were primarily constituted by high-affinity, low-capacity binding components in NFT-rich regions and low-affinity, high-capacity binding components in plaque-rich regions (Figures S9A and S9B). A subsequent simulation for radioligand binding in an area containing these two types of binding sites at a ratio of 1:1 indicated that the selectivity of [^{11}C]PBB3 for NFTs versus plaques may be inversely associated with concentration of free radioligands (Figure S9C). In a range of free concentration in the brain achievable

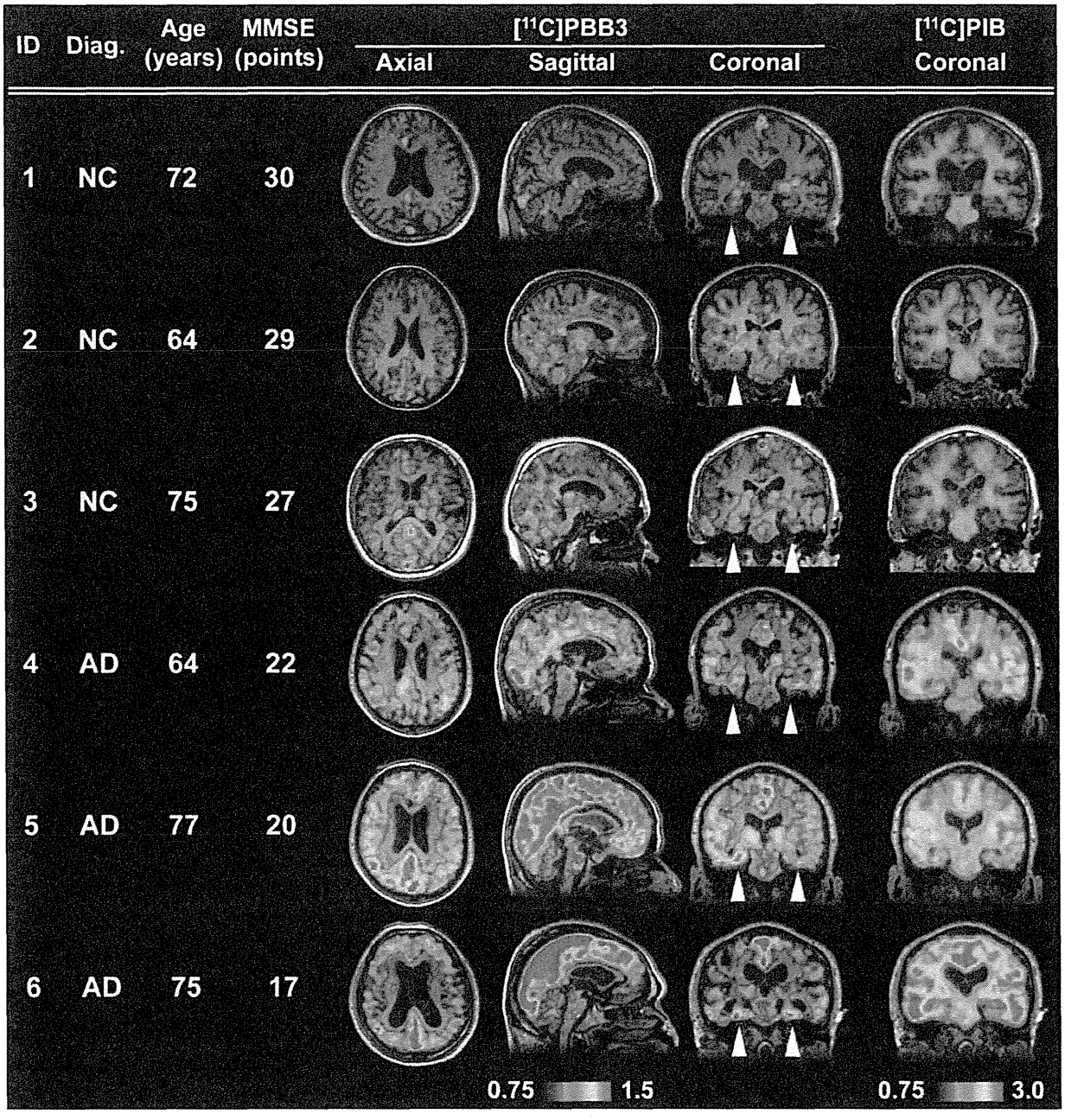

Figure 8. Orthogonal [^{11}C]PBB3-PET Images in All Human Subjects Examined in the Present Exploratory Clinical Study

Data are displayed as parametric maps for SUVR. The [^{11}C]PBB3 binding to the hippocampal formation (arrowheads) was increased consistently in AD patients in contrast to minimum radiotracer retention in normal control (NC) subjects with MMSE scores of 29–30 points (subjects 1 and 2). Another NC subject with an MMSE score of 27 points (subject 3) was negative for [^{11}C]PIB-PET but exhibited slight accumulation of radiotracer signals primarily around the hippocampus, resembling fibrillar tau deposition at Braak stage III/IV or earlier. Sagittal slices around the midline illustrate that radioligand signals were the most intense in the limbic system but began to expand to the neocortex in a patient with the mildest AD (subject 4), in agreement with the tau pathology at Braak stage V/VI, and was further intensified in most neocortical areas, corresponding to Braak stage VI, apparently as a function of the disease severity assessed by MMSE (subjects 5 and 6). The AD patient with the lowest MMSE score (subject 6) displayed a less profound increase of [^{11}C]PBB3 retention in the lateral temporal and parietal cortices than did the other two AD cases, and this is attributable to marked cortical atrophy in this individual and/or toxic loss of tau-bearing neurons in these brain areas at an advanced pathological stage. In contrast to the spatial profiles of [^{11}C]PBB3 binding, the distribution of [^{11}C]PIB signals appeared unchanged among AD subjects. See also Figure S9.

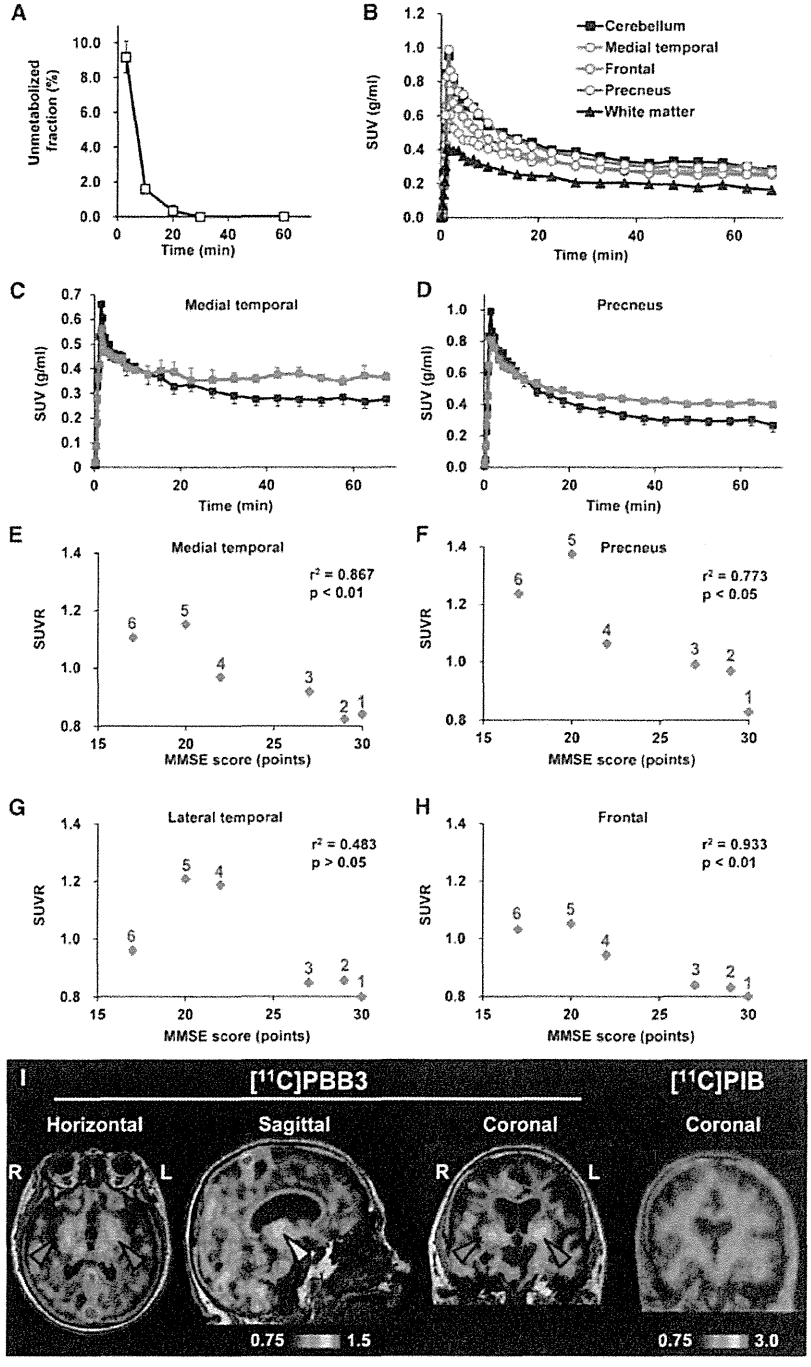

Figure 9. Pharmacokinetic Profiles of [^{11}C]PBB3 Administered to Humans and PET Images of a Patient Clinically Diagnosed as Having Corticobasal Syndrome

(A) Time course of unmetabolized [^{11}C]PBB3 fraction in plasma following intravenous radiotracer injection. The plot was generated by averaging data from six individuals.

(B) Time-radioactivity curves in different brain regions of cognitively normal control subjects over 70 min after intravenous injection of [^{11}C]PBB3. Data were generated by averaging values in two individuals and are presented as standard uptake values (SUVs).

(C and D) Comparisons of time-radioactivity curves in the medial temporal region (C) and precuneus (D) of normal controls (black symbols and lines; n = 3) and AD patients (red symbols and lines; n = 3).

(E–H) Scatterplots illustrating correlation of SUVRs with MMSE scores in the medial temporal region (E), precuneus (F), and lateral temporal (G) and frontal (H) cortices. Numbers beside symbols denote subject ID as indicated in Figure 8. Coefficients of determination (r^2) and p values by t test are displayed in graphs.

(I) [^{11}C]PBB3- and [^{11}C]PIB-PET images in a subject with clinical diagnosis of corticobasal syndrome. Images were generated as in Figures 7 and 8. Accumulation of [^{11}C]PBB3 was noticeable in the basal ganglia (red arrowheads) with right-side dominance and an area containing the thalamus and midbrain (yellow arrowhead).

Vertical bars in the graphs represent SEs. See also Figures S8 and S9.

at a pseudoequilibrium state in human PET imaging (<0.2 nM), [^{11}C]PBB3 is presumed to preferentially bind to tau lesions relative to in vitro autoradiographic (~1 nM) and fluorescence (>100 nM) labeling.

We also estimated contribution of [^{11}C]PBB3 bound to dense core plaques to total radiosignals in the neocortical gray matter of AD patients, by conducting autoradiography and FSB histochemistry for the same sections. Radiolabeling associated with dense cored plaques accounted for less than 1% and 3% of total gray matter signals in the temporal cortex and precuneus, respectively (Figures S9D–S9H). Moreover, fluorescence labeling of adjacent sections with PBB3 demonstrated that approximately 2% and 5% of total gray matter fluorescence signals were attributable to PBB3 bound to dense core plaques in the temporal cortex and precuneus, respectively. Hence, dense cored plaques were conceived to be rather minor sources of binding sites for [^{11}C]PBB3.

Finally, PET scans with [^{11}C]PBB3 and [^{11}C]PIB were conducted for a subject clinically diagnosed as having corticobasal syndrome. Retention of [^{11}C]PIB stayed at a control level, but notable accumulation of [^{11}C]PBB3 was observed in the neocortex and subcortical structures (Figure 9I), providing evidence for in vivo detection of tau lesions in plaque-negative

Please cite this article in press as: Maruyama et al., Imaging of Tau Pathology in a Tauopathy Mouse Model and in Alzheimer Patients Compared to Normal Controls, Neuron (2013), http://dx.doi.org/10.1016/j.neuron.2013.07.037

tauopathies. Interestingly, right-side dominant [^{11}C]PBB3-PET signals in the basal ganglia were consistent with laterality of atrophy in this area (Figure S8F). These findings may also be associated with a right-side dominant decrease in cerebral blood flow and left-side dominant motor signs in this patient.

DISCUSSION

Here, we report our efforts to develop BBB-penetrant ligands that are capable of binding to and visualizing intracellular tau aggregates in AD and non-AD tauopathies. These compounds may accordingly be useful for the differential diagnosis of neurological conditions in elderly subjects on the basis of the distribution of tau lesions, thereby opening up novel avenues for research in elucidating mechanisms of tau-mediated neurodegeneration, as well as tau-focused biomarkers and therapies.

Despite numerous efforts to develop imaging ligands to visualize tau pathologies in the brains of patients with AD and related tauopathies, the urgent need for these tau biomarkers remains largely unmet. To address this significant challenge, we also took advantage of a multimodal imaging system, which facilitates a quick and label-free validation of candidate compounds in terms of their transfer to the brain and retention in tau-rich regions. In addition, subcellular-resolution imaging optics exemplified by two-photon laser scanning microscopy provided proof of the rapid transfer of intravenously administered potential tau pathology imaging agents from plasma to the CNS extracellular matrix and subsequently to the cytoplasm of neurons, where they can bind to intracellular tau inclusions. Based on these encouraging preliminary data using nonlabeled compounds, a subset of these compounds was radiolabeled for use in PET imaging of Tg mice that model tau pathology, and a radioligand that yielded the best visualization of tau lesions in these Tg mice was selected for further testing in human AD patients and NC subjects as well as patients with probable CBD. This stepwise strategy enabled us to identify and advance the most promising PET probe for the visualization and quantitative assessment of tau pathology in the CNS of living human subjects. Interestingly, another research group has recently reported development of ^{18}F-labeled PET ligands for tau lesions mostly through assessments of binding to brain tissues, but not recombinant tau assemblies (Zhang et al., 2012; Chien et al., 2013), as in the present approach. These radioligands have been implied to produce considerably high contrasts for tau pathologies in living AD brains, and relatively long radioactive half-life of ^{18}F would enable delivery of radioligands from a radiosynthesis sites to multiple PET facilities. [^{11}C]PBB3 has distinct advantages over these compounds, as exemplified by affinity for diverse tau lesions, including Tg mouse tau aggregates, applicability to multimodal imaging, and induction of smaller radioactive exposure than ^{18}F-labeled ligands.

In the present work, we clinically validated the performance of [^{11}C]PBB3 as a tau imaging agent by comparing the distribution of [^{11}C]PBB3 with that of [^{11}C]PIB in AD brains. Tau deposits in patients with moderate or severe AD are thought to be distributed extensively in the neocortical and limbic regions (classified as Braak stage V/VI) (Braak and Braak, 1991), thereby resembling localization of senile plaques, except for the predominance of tau aggregates in the hippocampal formation. This rationalizes the use of radioactivity in the medial temporal area as an index to validate an imaging probe for tau pathology versus Aβ deposits in AD patients from prodromal to advanced stages. Furthermore, our preliminary data suggest that [^{11}C]PBB3 may be capable of capturing the temporospatial spreading of neurofibrillary tau pathologies from the limbic system (Braak stage III/IV or earlier) to neocortical areas (Braak stage V/VI) with the progression of AD (Figure 8). A considerable subset of tau lesions at Braak stage I/II is composed of phosphorylated tau deposits barely reactive with thioflavin-S (i.e., pretangles), and NFTs are relatively low in number and are confined to the transentorhinal cortex (Braak and Braak, 1991; Braak et al., 2011). Therefore, detection of these early tau pathologies would be more difficult. Our next-stage clinical study with expanded sample size and wider range of MMSE scores is currently ongoing to pursue tau accumulation in normal controls and subjects with mild cognitive impairments and AD at diverse stages and will bring more compelling insights into the significance of tau PET imaging in early diagnosis and prediction of AD. In addition, alterations of [^{11}C]PBB3 retention were indicated in the transition from mild to moderate AD. Loss of PET signals in the lateral temporal cortex of a patient with moderate AD (subject 6 in Figure 8) might not result from atrophy of this region, as the hippocampus of the same subject exhibited strong [^{11}C]PBB3 binding despite marked atrophy. Possible explanations for this change include formation of extracellular NFTs and their envelopment by astrocytes in the degenerating neocortex, profoundly modifying accessibility of these NFTs to exogenous molecules (Schmidt et al., 1988). This notion would need to be examined by combined autoradiogarphic and immunohistochemical assays of different brain regions.

Being able to visualize tau deposits with [^{11}C]PBB3 in non-AD tauopathies, such as PSP, CBD, and related disorders, is also of major importance, as suggested in the present PET data the support detectability of tau deposition in living CBD brains. As compared with NFTs and neuropil threads in AD, abundant tau deposits are largely confined to specific neuroanatomical locations of the CNS in tau-positive, plaque-negative illnesses, as exemplified by PSP and CBD (Dickson et al., 2011), but the homogenous and low-level background signals of [11C]PBB3 in brain parenchyma indicate the possibility of detecting tau lesions in these disorders. Following such in vivo assessments, a postmortem neuropathological evaluation of scanned subjects would be required as a reference standard for PET assays of non-AD tau pathologies.

[^{11}C]PIB-positive plaque formation nearly plateaus prior to the progression of brain atrophy in AD (Engler et al., 2006), but tau abnormalities may bridge the chasm between Aβ fibrillogenesis and neuronal death. Consistent with this notion, our PET/MRI data indicate that the deposition of tau inclusions as visualized by the intense [^{11}C]PBB3 labeling but lacking overt [^{11}C]PIB binding is closely associated with a local volume reduction in the hippocampal formation. Indeed, our pilot clinical PET study demonstrated that localized accumulation of [^{11}C]PBB3 in the medial temporal region of AD patients was accompanied by marked hippocampal atrophy (Figure 7B). Notably, [^{11}C]PBB3-PET signals were substantially increased, notwithstanding the atrophy-related partial volume effects on PET images, and this

observation may support the contribution of tau fibrils to toxic neuronal death in AD. However, these data do not immediately imply neurotoxicities of [^{11}C]PBB3-reactive tau fibrils, in light of MRI-detectable neurodegeneration uncoupled with [^{11}C]PBB3 retention in the hippocampus of PS19 mice. In the hippocampal formation of AD patients, neurons bearing NFTs that resemble those in the PS19 hippocampus may drive neurodegeneration similar to that observed in either the PS19 hippocampus or brain stem, and this issue could be addressed in future studies using [^{11}C]PBB3-PET and MRI in diverse mouse models, including PS19 and rTg4510 mice, and human subjects.

Our analyses of multiple β sheet ligands illustrated electrochemical and/or conformational diversities of β-pleated sheets among amyloid aggregates, producing a selectivity of these compounds for a certain spectrum of fibrillar pathologies (Figures 1 and S1). Lipophilicities of the β sheet ligands could determine their reactivity with noncored plaques, as noted among the PBBs studied here (Figure 1), although the molecular properties underlying this variation are yet to be elucidated. Meanwhile, we noted that all β sheet ligands tested in the present study were reactive with dense core plaques regardless of their lipophilicities. This may affect in vivo PET signals, particularly in AD brain areas with abundant cored plaques, such as the precuneus. However, our combined autoradiographic and histochemical assessments indicated that [^{11}C]PBB3 bound to dense core plaques accounts for less than 10% of total specific radioligand binding in these areas, and this percentage in fact includes binding to tau fibrils in plaque neurites in addition to Aβ amyloid core. A second possibility to account for the diversity of ligand reactivity to tau lesions may arise from the packing distance between two juxtaposed β sheets in tau filaments and is discussed in the Supplemental Discussion.

Notably, selectivity of [^{11}C]PBB3 for tau versus aggregates may depend on free radioligand concentration in the brain. Our autoradiographic binding assays suggested that affinity of [^{11}C]PBB3 for NFTs is 40- to 50-fold higher than senile plaques, but binding components on tau fibrils may be more readily saturated by this radioligand than those on Aβ fibrils. [^{11}C]PBB3-PET data in humans indicated that uptake of this radioligand into the brain is less than one-third of [^{11}C]PIB uptake and that free radioligand concentration in the brain at a pseudoequilibrium state is approximately 0.2 nM or lower. In this range of concentration, [^{11}C]PBB3 could preferentially interact with high-affinity binding components formed by tau assemblies. An excessive amount of radioligand in the brain would result in saturation of radioligand binding to tau lesions and increased binding to low-affinity, high-capacity binding components in Aβ plaques, and such overload of free radioligand is more likely in regions with less abundant tau pathologies. This could be even more critical in capturing early tau pathologies that originate in the hippocampal formation and may require technical improvements and methodological refinements, including high-resolution imaging, correction for motions of subjects during scans, and robust definition of VOIs on the atrophic hippocampus.

Although nonspecific [^{11}C]PBB3-PET signals in control human subjects were generally low, radioligand retention in dural venous sinuses was noticeable in all scanned individuals. Possible mechanisms that underlie this property are discussed in the Supplemental Discussion.

The present work has also implied the potential utility of multimodal imaging systems for translational development of therapeutic agents that counteract tau fibrillogenesis. Optical imaging with a near-infrared fluorescent probe, such as PBB5, could provide the least invasive technique to assess tau accumulation in living mouse models. As demonstrated by our in vitro and ex vivo fluorescence labeling, all PBBs share a similarity in terms of their reactivity with tau aggregates. Hence, PBB5 optics may be applicable to early screening of therapeutic agents that suppress tau deposition, and the data on abundance of tau lesions obtained by this approach may be translatable to advanced stages of assessments using [^{11}C]PBB3-PET in animal models and humans. By contrast, pharmacokinetic properties of PBB5 (Figure S5) were found to be distinct from those of electrically neutral PBBs, including PBB2 and PBB3. These considerations would be of importance in developing and using fluorescent ligands applicable to optical and PET imaging.

To conclude, our class of multimodal imaging agents offers the possibility of visual investigations of fibrillary tau pathologies at subcellular, cellular, and regional levels. These assay systems are potentially powerful tools for the longitudinal evaluation of anti-tau treatments (Marx, 2007), as a single probe may facilitate a seamless, bidirectional translation between preclinical and clinical insights. PET tracers would also serve a more immediate therapeutic purpose by enabling the assessment of the effects of anti-Aβ and anti-tau therapies on tau pathologies in living AD patients.

EXPERIMENTAL PROCEDURES

Compounds and Reagents

PBB1 (Wako Pure Chemical Industries), PBB2 (ABX), PBB3 (Nard Institute), PBB4 (ABX), mPBB5 (Nard Institute), desmethyl precursor of [^{11}C]PBB2 (2-[4-(4-aminophenyl)buta-1,3-dienyl]benzothiazol-6-ol; Nard Institute), desmethyl precursor of [^{11}C]PBB3 protected with a silyl group (5-[4-(6-tert-butyldimethylsilyloxy-benzothiazol-2-yl)buta-1,3-dienyl]pyridine-2-amine; Nard Institute), desmethyl precursor of [^{11}C]mPBB5 (2-[4-(4-dimethylaminophenyl) buta-1,3-dienyl]-3-ethyl-6-hydroxybenzothiazol-3-ium; Nard Institute), and 2-[8-(4-dimethylaminophenyl)octa-1,3,5,7-tetraenyl]-3-ethylbenzothiazol-3-ium (DM-POTEB; Nard Institute) were custom synthesized. Information on other chemicals is provided in the Supplemental Experimental Procedures. ClogP for each compound was calculated using ACD Chemsketch logP software (Advanced Chemistry Development).

Animal Models

Tg mice heterozygous for human T34 (4-repeat tau isoform with 1 N-terminal insert) with FTDP-17 P301S mutation driven by mouse prion protein promoter, also referred to as PS19 mice (Yoshiyama et al., 2007), were bred and kept on a C57BL/6 background. All mice studied here were maintained and handled in accordance with the National Research Council's Guide for the Care and Use of Laboratory Animals and our institutional guidelines. Protocols for the present animal experiments were approved by the Animal Ethics Committees of the National Institute of Radiological Sciences.

Postmortem Brain Tissues

Procedures for preparation of human and mouse brain sections are given in the Supplemental Experimental Procedures.

In Vitro and Ex Vivo Fluorescence Microscopy

Six micrometer paraffin sections generated from patient brains and 20 μm frozen sections of mouse brains were stained with 10^{-3}% β sheet ligands

dissolved in 50% ethanol for 1 hr at room temperature. Images of the fluorescence signals from these compounds were captured by nonlaser (BZ-9000; Keyence Japan) and confocal laser scanning (FV-1000; Olympus) microscopes. In the confocal imaging, excitation/emission wavelengths (nm) were optimized for each compound as follows: 405/420-520 (PBB3, FSB, PIB, BF-227, BF-158, FDDNP, thioflavin-S), 488/520-580 (PBB2, PBB4), 515/530-630 (PBB1, curcumin), and 635/645-720 (PBB5, BF-189, DM-POTEB). Subsequently, the tested samples and adjacent sections probed serially with each ligand were autoclaved for antigen retrieval, immunostained with the anti-tau monoclonal antibody AT8 that is specific for tau phosphorylated at Ser 202 and Thr 205 (Endogen), as well as a polyclonal antibody against AβN3(pE), and inspected using the microscopes noted above. For ex vivo imaging, PS19 and non-Tg WT at 10–12 months of age were anesthetized with 1.5% (v/v) isoflurane and were given 1 mg/kg PBB1-4, 0.1 mg/kg PBB5, or 10 mg/kg FSB by syringe via tail vein. The animals were killed by decapitation at 60 min after tracer administration. Brain and spinal cord were harvested and cut into 10-μm-thick sections on a cryostat (HM560). The sections were imaged using microscopes as in the in vitro assays and were labeled with either FSB or AT8, followed by microscopic re-examination.

Ex Vivo and In Vivo Multiphoton Imaging

Experimental procedures are given in the Supplemental Experimental Procedures.

In Vivo and Ex Vivo Pulsed Laser Scanning Imaging

Noninvasive scans of isoflurane-anesthetized non-Tg WT and tau Tg mice at 12 months of age were performed using a small animal-dedicated optical imager (eXplore Optix; ART). Scan protocols are given in the Supplemental Experimental Procedures.

Radiosynthesis of [^{11}C]PBB2

Experimental procedures are given in the Supplemental Experimental Procedures.

Radiosynthesis of [^{11}C]PBB3

[^{11}C]Methyl iodide was produced and transferred into 300 μl of dimethyl sulphoxide (DMSO) containing 1.5–2 mg of *tert*-butyldimethylsilyl desmethyl precursor and 10 mg of potassium hydroxide at room temperature. The reaction mixture was heated to 125°C and maintained for 5 min. After cooling the reaction vessel, 5 mg of *tetra-n*-butylammonium fluoride hydrate in 600 μl of water was added to the mixture to delete the protecting group, and then 500 μl of HPLC solvent was added to the reaction vessel. The radioactive mixture was transferred into a reservoir for HPLC purification (CAPCELL PAK C_{18} column, 10 × 250 mm; acetonitrile/50 mM ammonium formate = 4/6, 6 ml/min). The fraction corresponding to [^{11}C]PBB3 was collected in a flask containing 100 μl of 25% ascorbic acid solution and 75 μl of Tween 80 in 300 μl of ethanol and was evaporated to dryness under a vacuum. The residue was dissolved in 10 ml of saline (pH 7.4) to obtain [^{11}C]PBB3 (970–1,990 GBq at the end of synthesis [EOS]) as an injectable solution. The final formulated product was radiochemically pure (≥95%) as detected by analytic HPLC (CAPCELL PAK C_{18} column, 4.6 × 250 mm; acetonitrile/50 mM ammonium formate = 4/6, 2 ml/min). The specific activity of [^{11}C]PBB3 at EOS was 37–121 GBq/μmol, and [^{11}C]PBB3 maintained its radioactive purity exceeding 90% over 3 hr after formulation.

Radiosynthesis of [^{11}C]mPBB5

Experimental procedures are given as Supplemental Experimental Procedures.

Radiosynthesis of [^{11}C]PIB

Radiolabeling of PIB was performed as described elsewhere (Maeda et al., 2011). The specific activity of [^{11}C]PIB at EOS was 50–110 GBq/μmol.

In Vitro and Ex Vivo Autoradiography

Experimental procedures are given in the Supplemental Experimental Procedures.

In Vivo PET Imaging of Mice

PET scans were performed using a microPET Focus 220 animal scanner (Siemens Medical Solutions) immediately after intravenous injection of [^{11}C]PBB2 (28.3 ± 10.3 MBq), [^{11}C]PBB3 (29.7 ± 9.3 MBq), or [^{11}C]mPBB5 (32.8 ± 5.9 MBq). Detailed procedures are provided in the Supplemental Experimental Procedures.

In Vivo PET Imaging of Humans

Three cognitively normal control subjects (64, 72, and 75 years of age; mean age, 70.3 years) and three AD patients (64, 75 and 77 years of age; mean age, 72 years) were recruited to the present work (Figure 8). Additional information on these subjects is given in the Supplemental Experimental Procedures. The current clinical study was approved by the Ethics and Radiation Safety Committees of the National Institute of Radiological Sciences. Written informed consent was obtained from the subjects or their family members. PET assays were conducted with a Siemens ECAT EXACT HR+ scanner (CTI PET Systems). Detailed PET scan protocols are provided in the Supplemental Experimental Procedures. A fraction of radioactivity corresponding to unmetabolized [^{11}C]PBB3 in plasma at 3, 10, 20, 30, and 60 min was determined by HPLC (Waters mBondapak C_{18} column, 7.8 × 300 mm; acetonitrile/ammonium formate mobile phase with gradient elution = 40/60, 52/48, 80/20, 80/20, 40/60, and 40/60 at 0, 6, 7, 8, 9, and 15 min, respectively; flow rate, 6 ml/min) as described elsewhere (Suzuki et al., 1999). The radiotracer injection and following scans and plasma assays were conducted in a dimly lit condition to avoid photoracemization of the chemicals.

Individual MRI data were coregistered to the PET images using PMOD software (PMOD Technologies). Volumes of interest (VOIs) were drawn on coregistered MR images and were transferred to the PET images. Procedures of image analyses are provided in the Supplemental Experimental Procedures.

We additionally carried out PET scans of a patient who was clinically diagnosed as having corticobasal syndrome, as described in the Supplemental Experimental Procedures.

SUPPLEMENTAL INFORMATION

Supplemental Information includes Supplemental Experimental Procedures, nine figures, and one table and can be found with this article online at http://dx.doi.org/10.1016/j.neuron.2013.07.037.

ACKNOWLEDGMENTS

The authors thank Mr. T. Minamihisamatsu and Mr. Y. Matsuba for technical assistance, the staff of the Molecular Probe Group, National Institute of Radiological Sciences, for support with radiosynthesis, Dr. Y. Yoshiyama at National Hospital Organization Chiba-East Hospital for his support on clinical PET studies, and Dr. T. Iwatsubo at the University of Tokyo and Dr. H. Inoue at Kyoto University for their critical discussions. This work was supported in part by grants from the National Institute on Aging of the National Institutes of Health (AG10124 and AG17586) (to J.Q.T. and V. M.-Y.L.), Grants-in-Aid for Japan Advanced Molecular Imaging Program, Young Scientists (21791158) (to M.M.), Scientific Research (B) (23390235) (to M.H.), Core Research for Evolutional Science and Technology (to T.S.), Scientific Research on Innovative Areas ("Brain Environment") (23111009) (to M.H.) from the Ministry of Education, Culture, Sports, Science and Technology, Japan, Thomas H. Maren Junior Investigator Fund from College of Medicine, University of Florida (to N.S.), and research fund of Belfer Neurodegeneration Consortium (to Q.C. and M.-K.J.). M.M., H. Shimada, T.S., M.-R.Z., and M.H. are named as inventors on a patent application 0749006WO1, claiming subject matter related to the results described in this paper.

Accepted: July 12, 2013
Published: September 18, 2013

REFERENCES

Bacskai, B.J., Hickey, G.A., Skoch, J., Kajdasz, S.T., Wang, Y., Huang, G.F., Mathis, C.A., Klunk, W.E., and Hyman, B.T. (2003). Four-dimensional

multiphoton imaging of brain entry, amyloid binding, and clearance of an amyloid-β ligand in transgenic mice. Proc. Natl. Acad. Sci. USA *100*, 12462–12467.

Ballatore, C., Lee, V.M.Y., and Trojanowski, J.Q. (2007). Tau-mediated neurodegeneration in Alzheimer's disease and related disorders. Nat. Rev. Neurosci. *8*, 663–672.

Braak, H., and Braak, E. (1991). Neuropathological stageing of Alzheimer-related changes. Acta Neuropathol. *82*, 239–259.

Braak, H., Thal, D.R., Ghebremedhin, E., and Del Tredici, K. (2011). Stages of the pathologic process in Alzheimer disease: age categories from 1 to 100 years. J. Neuropathol. Exp. Neurol. *70*, 960–969.

Chien, D.T., Bahri, S., Szardenings, A.K., Walsh, J.C., Mu, F., Su, M.Y., Shankle, W.R., Elizarov, A., and Kolb, H.C. (2013). Early clinical PET imaging results with the novel PHF-tau radioligand [F-18]-T807. J. Alzheimers Dis. *34*, 457–468.

Dickson, D.W., Kouri, N., Murray, M.E., and Josephs, K.A. (2011). Neuropathology of frontotemporal lobar degeneration-tau (FTLD-tau). J. Mol. Neurosci. *45*, 384–389.

Engler, H., Forsberg, A., Almkvist, O., Blomquist, G., Larsson, E., Savitcheva, I., Wall, A., Ringheim, A., Långström, B., and Nordberg, A. (2006). Two-year follow-up of amyloid deposition in patients with Alzheimer's disease. Brain *129*, 2856–2866.

Fodero-Tavoletti, M.T., Okamura, N., Furumoto, S., Mulligan, R.S., Connor, A.R., McLean, C.A., Cao, D., Rigopoulos, A., Cartwright, G.A., O'Keefe, G., et al. (2011). ^{18}F-THK523: a novel *in vivo* tau imaging ligand for Alzheimer's disease. Brain *134*, 1089–1100.

Higuchi, M., Iwata, N., Matsuba, Y., Sato, K., Sasamoto, K., and Saido, T.C. (2005). ^{19}F and ^{1}H MRI detection of amyloid β plaques *in vivo*. Nat. Neurosci. *8*, 527–533.

Hintersteiner, M., Enz, A., Frey, P., Jaton, A.L., Kinzy, W., Kneuer, R., Neumann, U., Rudin, M., Staufenbiel, M., Stoeckli, M., et al. (2005). *In vivo* detection of amyloid-β deposits by near-infrared imaging using an oxazine-derivative probe. Nat. Biotechnol. *23*, 577–583.

Klunk, W.E., Wang, Y., Huang, G.F., Debnath, M.L., Holt, D.P., Shao, L., Hamilton, R.L., Ikonomovic, M.D., DeKosky, S.T., and Mathis, C.A. (2003). The binding of 2-(4′-methylaminophenyl)benzothiazole to postmortem brain homogenates is dominated by the amyloid component. J. Neurosci. *23*, 2086–2092.

Klunk, W.E., Engler, H., Nordberg, A., Wang, Y., Blomqvist, G., Holt, D.P., Bergström, M., Savitcheva, I., Huang, G.F., Estrada, S., et al. (2004). Imaging brain amyloid in Alzheimer's disease with Pittsburgh Compound-B. Ann. Neurol. *55*, 306–319.

Krebs, M.R.H., Bromley, E.H., and Donald, A.M. (2005). The binding of thioflavin-T to amyloid fibrils: localisation and implications. J. Struct. Biol. *149*, 30–37.

Kudo, Y., Okamura, N., Furumoto, S., Tashiro, M., Furukawa, K., Maruyama, M., Itoh, M., Iwata, R., Yanai, K., and Arai, H. (2007). 2-(2-[2-Dimethylaminothiazol-5-yl]ethenyl)-6- (2-[fluoro]ethoxy)benzoxazole: a novel PET agent for *in vivo* detection of dense amyloid plaques in Alzheimer's disease patients. J. Nucl. Med. *48*, 553–561.

Maeda, J., Ji, B., Irie, T., Tomiyama, T., Maruyama, M., Okauchi, T., Staufenbiel, M., Iwata, N., Ono, M., Saido, T.C., et al. (2007). Longitudinal, quantitative assessment of amyloid, neuroinflammation, and anti-amyloid treatment in a living mouse model of Alzheimer's disease enabled by positron emission tomography. J. Neurosci. *27*, 10957–10968.

Maeda, J., Zhang, M.R., Okauchi, T., Ji, B., Ono, M., Hattori, S., Kumata, K., Iwata, N., Saido, T.C., Trojanowski, J.Q., et al. (2011). *In vivo* positron emission tomographic imaging of glial responses to amyloid-beta and tau pathologies in mouse models of Alzheimer's disease and related disorders. J. Neurosci. *31*, 4720–4730.

Marx, J. (2007). Alzheimer's disease. A new take on tau. Science *316*, 1416–1417.

Okamura, N., Suemoto, T., Furumoto, S., Suzuki, M., Shimadzu, H., Akatsu, H., Yamamoto, T., Fujiwara, H., Nemoto, M., Maruyama, M., et al. (2005). Quinoline and benzimidazole derivatives: candidate probes for *in vivo* imaging of tau pathology in Alzheimer's disease. J. Neurosci. *25*, 10857–10862.

Santacruz, K., Lewis, J., Spires, T., Paulson, J., Kotilinek, L., Ingelsson, M., Guimaraes, A., DeTure, M., Ramsden, M., McGowan, E., et al. (2005). Tau suppression in a neurodegenerative mouse model improves memory function. Science *309*, 476–481.

Schmidt, M.L., Gur, R.E., Gur, R.C., and Trojanowski, J.Q. (1988). Intraneuronal and extracellular neurofibrillary tangles exhibit mutually exclusive cytoskeletal antigens. Ann. Neurol. *23*, 184–189.

Small, G.W., Kepe, V., Ercoli, L.M., Siddarth, P., Bookheimer, S.Y., Miller, K.J., Lavretsky, H., Burggren, A.C., Cole, G.M., Vinters, H.V., et al. (2006). PET of brain amyloid and tau in mild cognitive impairment. N. Engl. J. Med. *355*, 2652–2663.

Suzuki, K., Takei, M., and Kida, T. (1999). Development of an analyzing system for the sensitive measurement of radioactive metabolites on the PET study. J. Labelled Comp. Radiopharm. *42*, S658–S660.

Thompson, P.W., Ye, L., Morgenstern, J.L., Sue, L., Beach, T.G., Judd, D.J., Shipley, N.J., Libri, V., and Lockhart, A. (2009). Interaction of the amyloid imaging tracer FDDNP with hallmark Alzheimer's disease pathologies. J. Neurochem. *109*, 623–630.

Yang, L., Rieves, D., and Ganley, C. (2012). Brain amyloid imaging—FDA approval of florbetapir F18 injection. N. Engl. J. Med. *367*, 885–887.

Yoshiyama, Y., Higuchi, M., Zhang, B., Huang, S.M., Iwata, N., Saido, T.C., Maeda, J., Suhara, T., Trojanowski, J.Q., and Lee, V.M.Y. (2007). Synapse loss and microglial activation precede tangles in a P301S tauopathy mouse model. Neuron *53*, 337–351.

Zhang, W., Arteaga, J., Cashion, D.K., Chen, G., Gangadharmath, U., Gomez, L.F., Kasi, D., Lam, C., Liang, Q., Liu, C., et al. (2012). A highly selective and specific PET tracer for imaging of tau pathologies. J. Alzheimers Dis. *31*, 601–612.

Zhuang, Z.P., Kung, M.P., Hou, C., Skovronsky, D.M., Gur, T.L., Plössl, K., Trojanowski, J.Q., Lee, V.M.Y., and Kung, H.F. (2001). Radioiodinated styrylbenzenes and thioflavins as probes for amyloid aggregates. J. Med. Chem. *44*, 1905–1914.

JNNP Online First, published on October 16, 2013 as 10.1136/jnnp-2013-306110

RESEARCH PAPER

Apathy correlates with prefrontal amyloid β deposition in Alzheimer's disease

Takaaki Mori,[1,2] Hitoshi Shimada,[1,3] Hitoshi Shinotoh,[1,4] Shigeki Hirano,[1,5] Yoko Eguchi,[1] Makiko Yamada,[1] Ryuji Fukuhara,[2] Satoshi Tanimukai,[2] Ming-Rong Zhang,[1] Satoshi Kuwabara,[5] Shu-ichi Ueno,[1,2] Tetsuya Suhara[1]

▶ Additional material is published online only. To view please visit the journal online (http://dx.doi.org/10.1136/jnnp-2013-306110).

[1]Molecular Imaging Center, National Institute of Radiological Sciences, Chiba, Japan
[2]Department of Neuropsychiatry, Neuroscience, Ehime University Graduate School of Medicine, Shitsukawa, Toon City, Ehime, Japan
[3]Section for Human Neurophysiology, Research Center for Frontier Medical Engineering, Chiba University, Chiba, Japan
[4]Neurology Chiba, Chiba, Japan
[5]Department of Neurology, Chiba University Graduate School of Medicine, Chiba, Japan

Correspondence to
Tetsuya Suhara, Molecular Neuroimaging Program, Molecular Imaging Center, National Institute of Radiological Sciences, 4-9-1 Anagawa, Inage-ku, Chiba-shi, Chiba, 260-8555, Japan; suhara@nirs.go.jp

TM and HS are joint first authors.

To cite: Mori T, Shimada H, Shinotoh H, *et al. J Neurol Neurosurg Psychiatry* Published Online First: [*please include* Day Month Year] doi:10.1136/jnnp-2013-306110

ABSTRACT

Objective Neuropsychiatric symptoms affect many patients with Alzheimer's disease (AD). (^{11}C)Pittsburgh Compound-B (PIB) positron emission tomography (PET) has enabled the in vivo visualisation of brain amyloid-β (Aβ) deposition. This study exploratively investigated the correlation between brain Aβ deposition measured by (^{11}C)PIB PET and neuropsychiatric symptoms in AD.

Methods Participants were 28 patients (15 women, 13 men) with PIB-positive AD. Clinical assessments included Mini-Mental State Examination, Clinical Dementia Rating scale, neuropsychiatry inventory (NPI) and frontal assessment battery. All patients underwent three-dimensional T1-weighted MRI and (^{11}C)PIB PET. The distribution volume ratio (DVR), an index of (^{11}C)PIB retention and, thus, Aβ deposition, was estimated voxel by voxel from (^{11}C)PIB PET data with partial volume correction. Voxel-based correlation analysis was performed to assess the relationships between DVR and each NPI subscale. Additionally, voxel-based analysis of covariance (ANCOVA) of the DVR images was performed between Patients with AD with and without each neuropsychiatric symptom. Voxel-based morphometry analysis of MRI was also performed.

Results Apathy subscale was correlated with (^{11}C)PIB retention in the bilateral frontal and right anterior cingulate. (^{11}C)PIB retention was greater in the bilateral frontal cortex of patients with AD with apathy than those of without apathy. Overlapping areas between the two analyses were the bilateral orbitofrontal gyrus and left superior frontal gyrus. Other NPI subscales were not correlated with (^{11}C)PIB retention. Voxel-based morphometry analysis of MRI showed no significant cluster of correlation between grey matter volume and NPI subscales.

Conclusions This study revealed that prefrontal Aβ deposition correlates with apathy.

INTRODUCTION

Alzheimer's disease (AD) is the most common form of dementia, accounting for approximately 60% of all dementia cases.[1] AD is characterised by gradual deterioration of cognitive functions including memory, and neuropsychiatric symptoms affect as many as 88% of patients with AD.[2] These neuropsychiatric symptoms, including delusions, hallucinations, agitation, depression, anxiety, euphoria, apathy, disinhibition, irritability and aberrant motor behaviour,[3] have serious adverse consequences for patients and caregivers, such as greater impairment of daily living activities and deteriorating quality of life.[4]

In the last decades, neuroimaging measures, such as MRI, single-photon emission CT (SPECT) and ^{18}F-flurodeoxyglucose (FDG) positron emission tomography (PET) have revealed some correlations between neuropsychiatric symptoms and specific neural networks.[5] An MRI study revealed negative correlations between delusions and grey matter (GM) volumes in the left frontal lobe, right fronto-parietal cortex and left claustrum, between apathy and GM volumes in the anterior cingulate and bilateral frontal, and agitation and GM volumes in the left insula and bilateral anterior cingulate cortex.[5] Other FDG-PET studies demonstrated a correlation between apathy and the left orbitofrontal region[6] and bilateral anterior cingulate region.[7] Some SPECT studies reported that apathy was positively correlated with perfusion in prefrontal and anterior temporal cortices,[8] or the right amygdala, bilateral temporal, right posterior cingulate, right superior frontal, postcentral and left superior temporal gyrus.[9]

Meanwhile, the development of amyloid imaging radiotracers for PET, represented by (^{11}C) Pittsburgh Compound-B (PIB), has enabled the in vivo visualisation of brain amyloid-β (Aβ) deposition,[10] one of the core pathological features of AD. Aβ oligomers are the principal effectors of synaptic dysfunction and loss.[11] Postmortem study of AD has demonstrated strong positive correlation between the load of Aβ oligomers and cognitive decline.[12] Taken together, neuropsychiatric symptoms are correlated with regional brain damage, which could be related to neuronal toxicity of focal Aβ oligomers. Although (^{11}C)PIB PET does not detect Aβ oligomers, oligomers aggregate to form (^{11}C)PIB-detectable Aβ sheets and Aβ plaques. It has been demonstrated using (^{11}C)PIB PET that episodic memory impairment is related to Aβ deposition in the temporal cortex of patients with AD in the predementia stage.[13] However, to the best of our knowledge, there has been no study concerning the correlation between neuropsychiatric symptoms and brain Aβ deposition in patients with AD.

The aim of the present study was to investigate the correlation between brain Aβ deposition and neuropsychiatric symptoms in patients with AD exploratively by using (^{11}C)PIB PET with voxel-based whole-brain quantitative analysis.

METHODS

Subjects

Thirty-one persons clinically diagnosed with AD based on the National Institute of Neurological and Communicative Disease and Stroke/Alzheimer's Disease and Related Disorders Association (NINCDS-ADRDA) criteria were recruited.[14] Three of the patients with AD (9.7%) were diagnosed as PIB-negative by visual assessment of distribution volume ratio (DVR) images of (^{11}C)PIB PET (see method for creating DVR images) and were excluded. PIB-negative was defined as lower PIB uptake of any GM region than that of white matter (WM) by visual assessment of the DVR image. The 28 PIB-positive AD subjects were enrolled for further analyses.

Neuropsychiatric symptoms were assessed by neuropsychiatry inventory (NPI),[15] which is composed of 10 subscales: delusions, hallucinations, agitation, depression, anxiety, euphoria, apathy, disinhibition, irritability and aberrant motor behaviour. Subjects were also assessed by Mini-Mental State Examination (MMSE)[16] and Clinical Dementia Rating scale (CDR)[17] to measure the severity of global cognitive impairment, and by frontal assessment battery (FAB)[18] to measure the possible frontal dysfunction related to AD.[19]

The PET study was approved by the institutional review board of the National Institute of Radiological Sciences, Japan. Written informed consent was obtained from all subjects or from their spouses or other close family members.

Probe synthesis

(^{11}C)PIB was synthesised according to a previous method, by reaction of 2-(4′-aminophenyl)-6-hydroxy-benzothiazole and (^{11}C)methyl triflate.[20] The product had radiochemical purity greater than 96.2%. Specific activity ranged from 35.4 to 221.8 GBq/μ mol at the time of injection.

PET scan

PET images were acquired by Siemens ECAT EXACT HR+ scanner (CTI PET Systems, Knoxville, Tennessee, USA) with an axial field of view of 155 mm, providing 63 contiguous 2.46 mm slices, with 5.6 mm transaxial and 5.4 mm axial resolution. A 10 min transmission scan was performed to measure tissue attenuation. Dynamic emission scan data were acquired in three-dimensional mode for a period of 90 min. Subjects were examined with their eyes closed and their ears unplugged in a quiet room, and their heads were restrained with a band extending across the forehead attached to the headrest. An examiner carefully monitored head movement with laser beams during each scan, and corrections were made when necessary. A dose (370 ±34 MBq in 5 mL) of (^{11}C)PIB was intravenously injected for 60 s by infusion pump into the right cubital vein. The PET measurement protocol was based on a previously reported method,[20 21] with some modifications. Briefly, a sequence of 19 scans was acquired during 90 min (3×20 s, 3×40 s, 1×1 min, 2×3 min, 5×6 min, 5×10 min) after (^{11}C)PIB injection. All data processing and image reconstruction were performed using standard Siemens software including scatter correction.

MRI acquisition

MR images were obtained on 1.5 T Intera (Phillips Medical Systems, Best, The Netherlands) on the same day as the PET study. Subjects were scanned with a 3D T1-weighted turbo gradient echo sequence (repetition time (TR) range/echo time (TE) range, 16 msec/5.2 ms; field of view, 256 mm; matrix, 256×256; 196 contiguous axial slices of 1.0 mm thickness).

PET data analysis

Correction of (^{11}C)PIB PET data for partial volume effects was performed with an algorithm implemented in the PMOD software package (PMOD V.3.2; Technologies, Adliswil, Switzerland). This correction is based on the assumption that WM uptake is homogeneous. All brain pixels are classified as WM or GM and sorted into respective segments. Based on these segments and the assumed PET resolution, the spill-out from WM to GM can be estimated and subtracted. Similarly, the spill-out from GM to the surroundings can be estimated and compensated for. The result is a GM image with corrected activity values in all pixels. This method was introduced by Müller–Gärtner *et al.*[22] The parameters were performed as Point Spread Function FWHM: 2.0×2.0×2.0 mm, Correction mode: GM spill-out and spill-in. WM estimation: regression 0.95, and GM threshold: 0.3. All imaging data were then preprocessed and analysed with statistical parametric mapping software (SPM5, Wellcome Department of Cognitive Neurology, London, UK), operating in the Matlab software environment (V.7.10; MathWorks, Natick, Massachusetts, USA). Each T1-weighted MRI scan was coregistered to each PET image, and the spatial normalisation of the MRI images to the SPM5 T1 MRI template was applied to PET images.

A voxel-based DVR was estimated using Logan plot graphical analysis with the cerebellum as reference region by custom software designed by IDL (V.6.0; Jicoux Datasystems, Tokyo, Japan) from (^{11}C)PIB PET data.

First, a voxel-based correlation analysis was performed to assess the relationships between DVR and each NPI subscale using SPM5. Age, gender, education years, MMSE and FAB scores were also included in the model as covariates for all symptoms. Second, we performed voxel-based analysis of covariance (ANCOVA) of the DVR images between patients with AD with and without each neuropsychiatric symptom, adjusting for differences in age, gender, years of education, MMSE and FAB scores. FAB score was used as a covariate to remove the effects of frontal dysfunction, such as executive function and specific brain regions which are solely related to NPI symptoms.[19 23] Patients with AD with neuropsychiatric symptoms were defined with a cut-off score of 1 for each NPI subscale.

Voxel-based morphometry

We performed voxel-based morphometry to clarify the effect of GM atrophy, as a past study reported that GM atrophy was associated with some neuropsychiatric symptoms.[6] T1-weighted images were segmented into GM, WM and cerebrospinal fluid. In SPM5, spatial normalisation, segmentation and modulation are processed by means of a unified segmentation algorithm using SPM5.[24 25] The segmented and modulated normalised GM images were smoothed with a 12 mm FWHM Gaussian kernel. Total intracranial volume (TIV) was computed using the native-space tissue maps of each subject. TIV was included in the model as covariate in the voxel-based morphometry (VBM) analyses. The correlations between GM volumes and each NPI subscale were also analysed. Additionally, ANCOVA of GM volumes between patients with AD with and without neuropsychiatric symptoms was performed. In these analyses, besides TIV, age, gender and education years, also included in the model as covariates were the MMSE and FAB scores.

Statistical analysis

Group comparisons in demographic variables were performed by Fisher's exact test for gender ratio and CDR, and Student t test for

the others. Statistical analyses were performed using Statistical Package for the Social Sciences software (SPSS V.19, SPSS, Chicago, Illinois, USA). In SPM voxel-based correlation analyses and ANCOVA analyses, false discovery rate (FDR) corrected, $p<0.05$ was considered significant. The extent thresholds were defined as >500 in correlation analyses, and >200 in ANCOVA.

RESULTS

Twenty-eight patients with AD (15 women, 13 men), aged from 56 to 85 years, were the participants in this study. Their demographic and clinical data are presented in table 1, and their neuropsychiatric symptoms are shown in table 2. Apathy was the most frequent neuropsychiatric symptom (39.2%), while hallucinations and euphoria were rare (7.1%).

Voxel-based correlation analysis of (^{11}C)PIB DVR images showed that apathy subscale was significantly correlated with (^{11}C)PIB retention in the bilateral middle frontal gyrus, bilateral orbitofrontal gyrus, bilateral medial frontal gyrus, bilateral inferior frontal gyrus, bilateral superior fontal gyrus, bilateral insula, and right anterior cingulate gyrus (FDR, corrected $p<0.05$, cluster extent >500 voxels, voxel size: 2×2×2 mm) (table 3, figure 1). Additionally, the correlation between NPI apathy scale and prefrontal. (^{11}C)PIB DVR was confirmed in the volume of interest analysis without partial volume correction ($r^2=0.374$, $p<0.05$, see online supplementary figure E-1). SPM analysis did not show any significant cluster of correlation between any other neuropsychiatric symptom subscale and (^{11}C)PIB retention except apathy.

Voxel-based ANCOVA of the DVR images between patients with AD with and without each of the neuropsychiatric symptoms showed greater (^{11}C)PIB retention in 11 patients with AD with apathy in the bilateral superior frontal gyri, bilateral orbitofrontal gyri, bilateral medial frontal gyri, right middle frontal gyrus, and right middle temporal gyrus than in the 17 without apathy (FDR, corrected $p<0.05$, cluster extent >200 voxels, voxel size: 2×2×2 mm) (figure 2). There were no significant differences in gender, MMSE, education, FAB, NPI, disease duration and CDR (all $p>0.05$), and only age of the patients with AD with apathy was significantly lower compared with those without ($p<0.01$) (table 4). Voxel-based ANCOVA did not show any significant (^{11}C)PIB retention cluster in other neuropsychiatric symptoms except apathy. The overlapping areas between correlation and two-sample analyses were the bilateral orbitofrontal gyri and left superior frontal gyrus (figure 3).

SPM analysis of T1-weighted MRI did not show any significant cluster of correlation between GM volume and any NPI subscale score. Voxel-by-voxel ANCOVA of GM volume between patients with AD with and without neuropsychiatric symptoms did not show any significant cluster in any neuropsychiatric subscale.

Table 1 Demographics and clinical scores

	Mean (SD)
Age (years)	73.9 (7.9)
Gender (F/ M)	15/13
MMSE	19.9 (5.1)
Education (years)	11.1 (3.5)
CDR score (0:0.5:1:2:3)	0:15:9:3:1
FAB	12.1 (3.3)
NPI	4.6 (5.0)
Disease duration (years)	2.8 (1.6)

CDR, Clinical Dementia Rating scale; FAB, frontal assessment battery; MMSE, Mini-Mental State Examination; NPI, neuropsychiatry inventory.

Table 2 Prevalence and scores of NPI subscales

	Symptom-presenting subjects	NPI score of all subjects	NPI score of symptom-presenting subjects	
	n (%)	Mean (SD)	Mean (SD)	Range
Delusions	4 (14.2)	0.25 (0.79)	1.75 (1.50)	1–4
Hallucinations	2 (7.1)	0.10 (0.41)	1.50 (0.70)	1–2
Agitation	6 (21.4)	0.60 (1.66)	2.83 (2.71)	1–8
Depression	7 (25.0)	0.71 (1.73)	2.85 (2.54)	1–3
Anxiety	6 (21.4)	0.25 (0.51)	1.16 (0.40)	1–2
Euphoria	2 (7.1)	0.07 (0.26)	1.00 (0.00)	1–1
Apathy	11 (39.2)	1.28 (2.03)	3.27 (2.00)	1–8
Disinhibition	4 (14.2)	0.17 (0.47)	1.25 (0.50)	1–2
Irritability	9 (32.1)	0.85 (1.77)	2.66 (2.31)	1–8
Aberrant motor behaviour	4 (14.2)	0.35 (1.06)	2.50 (1.73)	1–4
NPI total	24 (85.7)	4.67 (5.02)	5.45 (5.02)	1–25

Number (%) and scores of NPI subscales of Alzheimer's disease patients. Apathy was the most frequent neuropsychiatric symptom (39.2%), while hallucinations and euphoria were rare (7.1%).
NPI, neuropsychiatry inventory.

DISCUSSION

We performed an exploratory study of the correlation between (^{11}C)PIB retention and neuropsychiatric symptoms. We introduced a cross-validation approach to detect any robust relationship between them. A positive correlation was found between apathy severity and (^{11}C)PIB retention in the bilateral superior, middle and inferior frontal gyri; bilateral orbitofrontal gyri, bilateral medial frontal gyri, bilateral insula and right anterior cingulate gyrus. Moreover, patients with AD with apathy showed increased (^{11}C)PIB retention in the bilateral superior frontal gyri, bilateral orbitofrontal gyri, bilateral medial frontal gyri, right middle frontal gyrus, and right middle temporal gyrus, when compared with those without apathy. Overlapping areas were the bilateral orbitofrontal gyri and left superior frontal gyrus. We did not find any significant correlation between GM volume and neuropsychiatric symptoms. This is the first study to reveal the correlation between brain Aβ deposition and neuropsychiatric symptoms in patients with AD by the use of (^{11}C)PIB PET with voxel-based whole-brain quantitative analysis.

Several neuroimaging studies have reported the specific brain region responsible for apathy in patients with AD. Previous FDG PET studies reported reduced glucose metabolism in the bilateral anterior cingulate region extending inferiorly to the medial orbitofrontal region and bilateral medial thalamus,[7] or hypometabolism in left orbitofrontal regions[6] in patients with AD with apathy compared with those without. SPECT studies reported that patients with AD with apathy were associated with hypoperfusion in prefrontal and anterior temporal cortices,[8] or the right amygdala, bilateral temporal, right posterior cingulate, right superior frontal, postcentral and left superior temporal gyri.[9] An MRI study reported greater cortical thinning in the left caudal anterior cingulate cortex and left lateral orbitofrontal cortex, and left superior and ventrolateral frontal regions in patients with AD with apathy than in those without.[26] Another MRI study revealed that apathy was

Table 3 Location, Z score and cluster size of significantly positive correlation between apathy and (^{11}C) Pittsburgh Compound-B (PIB) retention

		Peak coordinates (MNI)				
	Brodmann area	X	y	z	Z score	Cluster size
Right middle frontal gyrus*	8	26	20	42	5.33	1960
Right anterior cingulate gyrus	32	18	12	44	4.66	1960
Right medial frontal gyrus	8	14	32	40	4.24	1960
Right superior frontal gyrus	10	20	60	8	3.21	1960
Left orbitofrontal gyrus	11	−4	40	−26	3.03	1960
Right orbitofrontal gyrus	11	16	54	−16	2.99	1960
Right inferior frontal gyrus	44	50	8	24	4.61	1544
Right insula	13	50	−22	26	4.36	1544
Left medial frontal gyrus	8	−12	24	44	4.17	990
Left middle frontal gyrus	8	−24	26	44	3.87	990
Left superior frontal gyrus	6	−12	6	60	3.70	990
Left insula	13	−36	16	10	3.93	604
Left inferior frontal gyrus	47	−36	32	4	3.70	604

Voxel-based positron emission tomography image correlation analysis showed that apathy subscale was significantly correlated with (^{11}C)PIB retention (FDR-corrected p<0.05, extent threshold >500 voxels).
*Family-wise error (FWE)–corrected, p<0.05, extent threshold >200 voxels.
FDR, false discovery rate; MNI, Montreal Neurological Institute.

associated with GM density loss in the bilateral anterior cingulate and bilateral frontal cortex, head of the left caudate nucleus and the bilateral putamen in patients with AD.[5] There is evidence that regional patterns of amyloid deposition may not match the patterns of glucose metabolism or GM loss in the brain of AD.[27 28] However, we found a relationship between apathy and (^{11}C)PIB retention in the bilateral orbitofrontal gyri and right superior frontal gyrus of patients with AD, which was in agreement with these prior neuroimaging findings in terms of brain regions.[5–9]

A neuropathological study demonstrated that chronic apathy and total NPI composite scores were correlated with anterior cingulate neurofibrillary tangles, but not neuritic plaques in AD brains,[29] a result discordant with our findings. This discrepancy could be explained by the fact that AD brains were obtained at an advanced disease stage in the neuropathological study, while

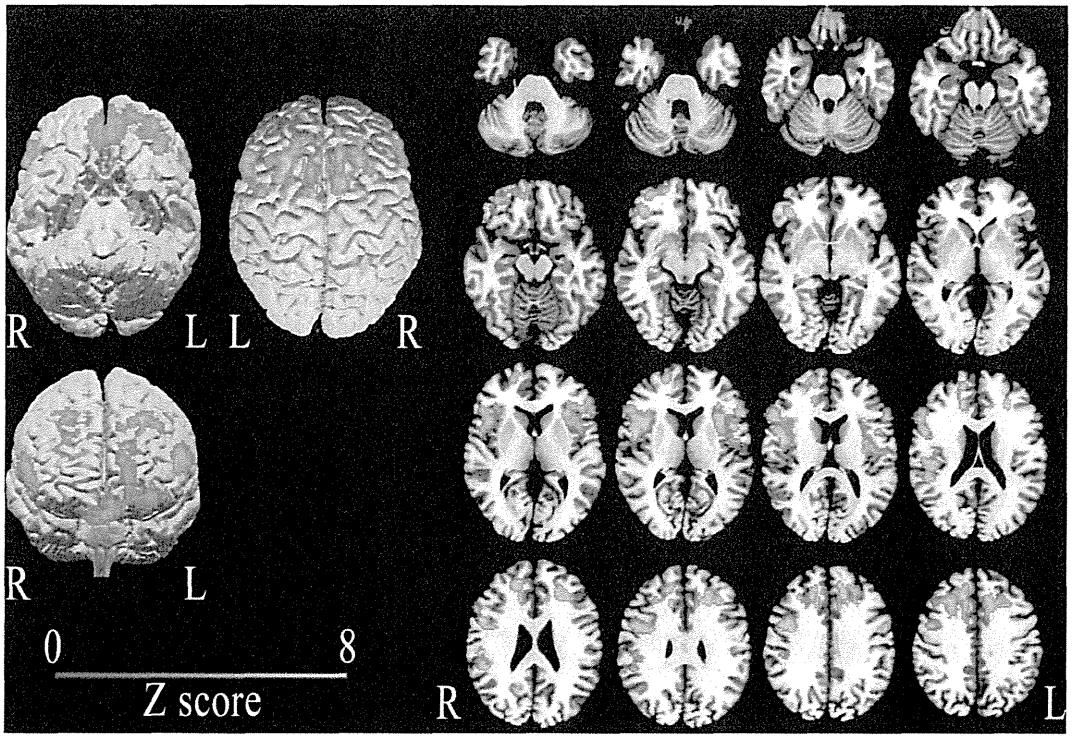

Figure 1 Images of voxel-based maps of significant correlation between neuropsychiatry inventory apathy score and (^{11}C) Pittsburgh Compound-B (PIB) retention (false discovery rate, corrected p<0.05, extent threshold >500 voxels). On the left are render images, and on the right axial images. Apathy score was significantly correlated with (^{11}C)PIB retention in bilateral middle frontal gyri, bilateral orbitofrontal gyri, bilateral medial frontal gyri, bilateral inferior frontal gyri, bilateral superior fontal gyri, bilateral insula and right anterior cingulate gyrus.

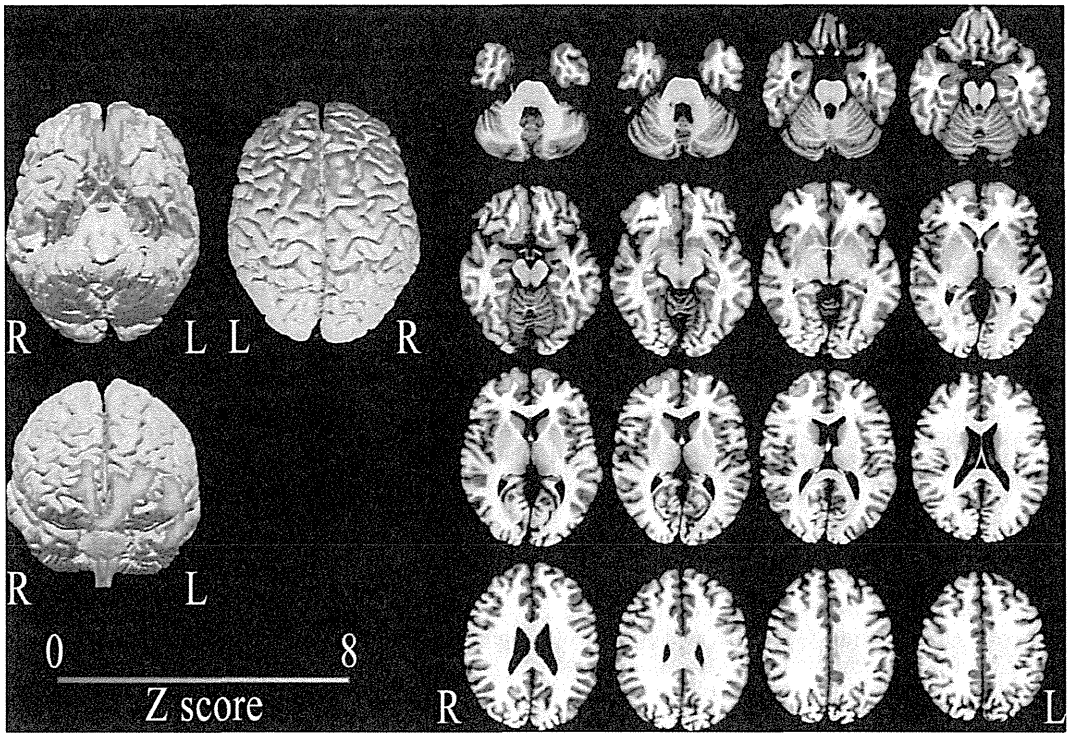

Figure 2 Images voxel-based maps with more (^{11}C) Pittsburgh Compound-B (PIB) retention in the Alzheimer's disease (AD) group with apathy than in the AD group without apathy by ANCOVA (false discovery rate, corrected p<0.05, extent threshold >200 voxels). On the left are render images, and on the right axial images. (^{11}C)PIB retention of patients with AD with apathy was greater in the bilateral superior frontal gyri, bilateral orbitofrontal gyri, bilateral medial frontal gyri, right middle frontal gyrus and right middle temporal gyrus than in those without apathy.

we measured Aβ deposition in patients with AD in the early disease stage in vivo.

In vitro and in vivo studies have shown that Aβ oligomers reduce glutamatergic synaptic transmission strength and plasticity,[30] and in mice transgenic for human amyloid precursor protein, pathologically elevated levels of Aβ promote the formation of pathogenic Aβ oligomers and cause wide fluctuations in the neuronal expression of synaptic activity-regulated genes,[31] epileptiform activity and non-convulsive seizures.[31] Aβ deposition also increases the proportion of abnormally hyperactive neurons in cortical circuits.[32] (^{11}C)PIB has been demonstrated to bind to fibrillar Aβ in diffuse, cored and neuritic plaques, but not to Aβ oligomers,[33] whereas, Aβ oligomers aggregate to form Aβ sheets and Aβ plaques. Therefore, brain regions with high (^{11}C)PIB retention could have greater amounts of Aβ oligomers than brain regions with modest (^{11}C)PIB retention at least in the early or preclinical stage of AD. It has been demonstrated that healthy elderly individuals with high (^{11}C)PIB retention show accelerated cortical atrophy, suggesting that the Aβ load is toxic to local brain regions at the preclinical stage of AD. Taken together, prominent Aβ deposition in the orbitofrontal and superior frontal gyri is thought to play a role in the neuropsychiatric symptom of apathy in patients with AD in the present study.

Table 4 Demographics and clinical scores of apathy-present group and apathy-free group

	AD group with apathy (n=11) Mean (SD)	AD group without apathy (n=17) Mean (SD)	p Value
Age	68.5 (7.9)	77.4 (5.9)	<0.01
Gender (M/F)	5/6	8/9	1.00
MMSE	18.0 (4.7)	21.1 (5.1)	0.12
Education	10.9 (3.6)	11.2 (3.5)	0.78
CDR score (0:0.5:1:2:3)	0:4:5:1:1	0:11:4:2:0	0.25
FAB	11.0 (3.3)	12.7 (3.2)	0.20
NPI total score	5.9 (3.4)	3.8 (5.7)	0.30

Age, MMSE, education, FAB, NPI total score were examined using Student t test. Gender and CDR sore were examined using Fisher's exact test.
AD, Alzheimer's disease; CDR, Clinical Dementia Rating scale; FAB, frontal assessment battery; MMSE, Mini-Mental State Examination; NPI, neuropsychiatry inventory.

In this study, we demonstrated that Aβ deposition in the orbitofrontal and superior frontal gyri is related to apathy in patients with AD, while GM volume in those areas was not correlated with apathy in patients with AD, or differed between patients with AD with and without apathy. The current hypothetical model suggests that Aβ peptide accumulation is a key early event in the pathophysiological process of AD, followed by synaptic dysfunction identified by FDG PET, and subsequent neural loss demonstrated by structural MRI progresses.[34 35] Increased (^{11}C)PIB retention in the frontal cortex may be an early marker of cortical damage in AD, and apparent atrophy may follow as the disease progresses. Another possible cause for the absent correlation between GM volume and apathy in this study may be that the AD group without apathy was older than the AD group with apathy.

It has been established that damage of the anterior cingulate circuit presents with apathy,[36] and that the neurons project to the ventral striatum that includes the olfactory tubercle.[36] The function of the anterior cingulate cortex relates to the initiation

Figure 3 Overlapped (^{11}C) Pittsburgh Compound-B retention area between correlation and ANCOVA analyses in apathy. The bilateral orbitofrontal gyrus and left superior frontal gyrus are correlated with apathy in Alzheimer's disease.

and motivational drivers for goal-directed activities, and therefore, damage to this cortical structure would likely lead to a degree of behavioural and cognitive inertia.[37 38] The orbitofrontal afferents provide information regarding the emotional relevance of external stimuli to the anterior cingulate circuit from internal and external environments,[36] and the medial orbitofrontal region has mutual connections with the anterior cingulate and medial dorsal nucleus of the thalamus.[39] Cholinergic neurons originate from the basal nucleus of Meynert and project to frontal limbic cortical regions.[39] Cholinergic dysfunction may also contribute to apathy, because some studies have demonstrated that cholinesterase inhibitors improved apathy in patients with AD.[40]

A previous study using MRI demonstrated that delusions were associated with decreased GM density in the left frontal lobe, right frontoparietal cortex and left claustrum, and agitation was associated with decreased GM volumes in the left insula and bilateral anterior cingulate cortex.[5] Another study using FDG-PET reported that depression was associated with hypometabolism in bilateral dorsolateral prefrontal regions.[6] We did not find any correlation between (^{11}C)PIB retention and other neuropsychiatric symptoms except apathy, which probably resulted from the lack of, or only mild symptoms of, delusion, agitation and depression in the patients with AD in the present study.

The limitations of this exploratory study are its small sample size, and mild NPI symptoms including apathy. Although apathy was the most prevalent symptom, less than half the subjects exhibited apathy in this study. PIB retention is well known to have a predilection for the frontal lobes. Taken together, a correlation observed with overall mild NPI apathy symptoms might suggest that frontal PIB retention is a sensitive marker of apathy symptoms, but not necessarily a very specific one. Further studies in a larger number of patients with AD with NPI symptoms will be needed to confirm the correlation between prefrontal (^{11}C)PIB retention and the severity of apathy, and reveal a correlation with (^{11}C)PIB retention and other neuropsychiatric symptoms besides apathy, which may help to clarify the involved mechanisms and brain circuits, and lead to new insights into the pathophysiology of patients with AD.

Contributors Study concept/design: TM, HShim, HShin, SHira. Data analysis/interpretation: TM, HShim, HShin, SHira, YE. Manuscript preparation: TM, HShim, HShin, SHira, YE, MY, RF, ST, M-RZ, SK, S-cU, TS.

Funding Dr Kuwabara is funded by Grants-in-Aid for Scientific Research from the Ministry of Education, Culture, Sports, Science and Technology of Japan (23591267, 20590988, 20591018, 23591269), and a Grant-in-Aid for Scientific Research from the Ministry of Health, Labour and Welfare of Japan (JMA-IIA00046), and serves as Associate Editor of *'Journal of Neurology, Neurosurgery, and Psychiatry'*, Editor of *'Internal Medicine'*, and Editorial Board member of *'Clinical Neurophysiology'*. Dr Ueno is funded by a Health and Labour Science Research Grant from the Japanese Ministry of Health, Labour and Welfare, and a Grant-in-Aid for Scientific Research from the Japanese Ministry of Education, Culture, Sports, Science and Technology (23659567). Dr Suhara is funded by the Ministry of Education, Culture, Sports, Science and Technology of Japan, the Strategic Research Program for Brain Sciences and Molecular Imaging Program, and serves as an Editorial Board member of *'International Journal of Neuropsychopharmacology'*, *'Psychogeriatrics'* and *'Current Psychiatry Review'*.

Competing interests A part of this study is the result of 'Integrated research on neuropsychiatric disorders' carried out under the Strategic Research Program for Brain Sciences by the Ministry of Education, Culture, Sports, Science and Technology of Japan, 'Japan Advanced Molecular Imaging Program (J-AMP)' of the Ministry of Education, Culture, Sports, Science and Technology (MEXT), Japan, a Grant-in-Aid for Scientific Research on Innovative Areas from the Ministry of Education, Culture, Sports, Science and Technology, Japan, and a Grant-in-Aid for Comprehensive Research on Dementia (No. 11103404) from the Ministry of Health, Labour and Welfare, Japan.

Patient consent Obtained.

Ethics approval The Institutional Review Board of the National Institute of Radiological Sciences.

Provenance and peer review Not commissioned; externally peer reviewed.

REFERENCES

1 Small GW, Rabins PV, Barry PP, *et al*. Diagnosis and treatment of Alzheimer disease and related disorders. Consensus statement of the American Association for Geriatric Psychiatry, the Alzheimer's Association, and the American Geriatrics Society. *JAMA* 1997;278:1363–71.
2 Mega MS, Cummings JL, Fiorello T, *et al*. The spectrum of behavioral changes in Alzheimer's disease. *Neurology* 1996;46:130–5.
3 Frisoni GB, Rozzini L, Gozzetti A, *et al*. Behavioral syndromes in Alzheimer's disease: description and correlates. *Dement Geriatr Cogn Disord* 1999;10:130–8.
4 González-Salvador T, Lyketsos CG, Baker A, *et al*. Quality of life in dementia patients in long-term care. *Int J Geriatr Psychiatry* 2000;15:181–9.
5 Bruen PD, McGeown WJ, Shanks MF, *et al*. Neuroanatomical correlates of neuropsychiatric symptoms in Alzheimer's disease. *Brain* 2008;131:2455–63.
6 Holthoff VA, Beuthien-Baumann B, Kalbe E, *et al*. Regional cerebral metabolism in early Alzheimer's disease with clinically significant apathy or depression. *Biol Psychiatry* 2005;57:412–21.
7 Marshall GA, Monserratt L, Harwood D, *et al*. Positron emission tomography metabolic correlates of apathy in Alzheimer disease. *Arch Neurol* 2007;64:1015–20.
8 Craig AH, Cummings JL, Fairbanks L, *et al*. Cerebral blood flow correlates of apathy in Alzheimer disease. *Arch Neurol* 1996;53:1116–20.
9 Kang JY, Lee JS, Kang H, *et al*. Regional cerebral blood flow abnormalities associated with apathy and depression in Alzheimer disease. *Alzheimer Dis Assoc Disord* 2012;26:217–24.
10 Klunk WE, Engler H, Nordberg A, *et al*. Imaging brain amyloid in Alzheimer's disease with Pittsburgh Compound-B. *Ann Neurol* 2004;55:306–19.
11 Walsh DM, Klyubin I, Fadeeva JV, *et al*. Naturally secreted oligomers of amyloid beta protein potently inhibit hippocampal long-term potentiation in vivo. *Nature* 2002;416:535–9.
12 Näslund J, Haroutunian V, Mohs R, *et al*. Correlation between elevated levels of amyloid beta-peptide in the brain and cognitive decline. *JAMA* 2000;283:1571–7.
13 Chételat G, Villemagne VL, Pike KE, *et al*. Independent contribution of temporal beta-amyloid deposition to memory decline in the pre-dementia phase of Alzheimer's disease. *Brain* 2011;134:798–807.
14 McKhann G, Drachman D, Folstein M, *et al*. Clinical diagnosis of Alzheimer's disease: report of the NINCDS-ADRDA Work Group under the auspices of Department of Health and Human Services Task Force on Alzheimer's Disease. *Neurology* 1984;34:939–44.
15 Cummings JL, Mega M, Gray K, *et al*. The Neuropsychiatric Inventory: comprehensive assessment of psychopathology in dementia. *Neurology* 1994;44:2308–14.
16 Folstein MF, Folstein SE, McHugh PR. Mini-mental state. A practical method for grading the cognitive state of patients for the clinician. *J Psychiatr Res* 1975;12:189–98.
17 Morris JC. The Clinical Dementia Rating (CDR): current version and scoring rules. *Neurology* 1993;43:2412–4.
18 Dubois B, Slachevsky A, Litvan I, *et al*. The FAB: a frontal assessment battery at bedside. *Neurology* 2000;55:1621–26.
19 Starr JM, Lonie J. Relationship between behavioural and psychological symptoms of dementia and cognition in Alzheimer's disease. *Dement Geriatr Cogn Disord* 2007;24:343–7.

20 Price JC, Klunk WE, Lopresti BJ, *et al*. Kinetic modeling of amyloid binding in humans using PET imaging and Pittsburgh Compound-B. *J Cereb Blood Flow Metab* 2005;25:1528–47.
21 Lopresti BJ, Klunk WE, Mathis CA, *et al*. Simplified quantification of Pittsburgh Compound B amyloid imaging PET studies: a comparative analysis. *J Nucl Med* 2005;46:1959–72.
22 Müller-Gärtner HW, Links JM, Prince JL, *et al*. Measurement of radiotracer concentration in brain gray matter using positron emission tomography: MRI-based correction for partial volume effects. *J Cereb Blood Flow Metab* 1992; 12:571–83.
23 Yamao A, Nagata T, Shinagawa S, *et al*. Differentiation between amnestic-mild cognitive impairment and early-stage Alzheimer's disease using the Frontal Assessment Battery test. *Psychogeriatrics* 2011;11:235–41.
24 Ashburner J, Friston KJ. Unified segmentation. *Neuroimage* 2005;26:839–51.
25 Ashburner J, Friston KJ. Voxel-based morphometry–the methods. *Neuroimage* 2000;1:805–21.
26 Tunnard C, Whitehead D, Hurt C, *et al*. Apathy and cortical atrophy in Alzheimer's disease. *Int J Geriatr Psychiatry* 2011;26:741–8.
27 Edison P, Archer HA, Hinz R, *et al*. Amyloid, hypometabolism, and cognition in Alzheimer disease: an [11C]PIB and [18F]FDG PET study. *Neurology* 2007;68:501–8.
28 Frisoni GB, Lorenzi M, Caroli A, *et al*. In vivo mapping of amyloid toxicity in Alzheimer disease. *Neurology* 2009;72:1504–11.
29 Marshall GA, Fairbanks LA, Tekin S, *et al*. Neuropathologic correlates of apathy in Alzheimer's disease. *Dement Geriatr Cogn Disord* 2006;21:144–7.
30 Chapman PF, White GL, Jones MW, *et al*. Impaired synaptic plasticity and learning in aged amyloid precursor protein transgenic mice. *Nat Neurosci* 1999;2:271–6.
31 Palop JJ, Chin J, Roberson ED, *et al*. Aberrant excitatory neuronal activity and compensatory remodeling of inhibitory hippocampal circuits in mouse models of Alzheimer's disease. *Neuron* 2007;55:697–711.
32 Busche MA, Eichhoff G, Adelsberger H, *et al*. Clusters of hyperactive neurons near amyloid plaques in a mouse model of Alzheimer's disease. *Science* 2008;321:1686–9.
33 Beckett TL, Webb RL, Niedowicz DM, *et al*. Postmortem Pittsburgh Compound B (PiB) binding increases with Alzheimer's disease progression. *J Alzheimers Dis* 2012;32:127–38.
34 Jack CR Jr, Knopman DS, Jagust WJ, *et al*. Hypothetical model of dynamic biomarkers of the Alzheimer's pathological cascade. *Lancet Neurol* 2010; 9:119–28.
35 Sperling RA, Aisen PS, Beckett LA, *et al*. Toward defining the preclinical stages of Alzheimer's disease: recommendations from the National Institute on Aging-Alzheimer's Association workgroups on diagnostic guidelines for Alzheimer's disease. *Alzheimers Dement* 2011;7:280–92.
36 Tekin S, Cummings JL. Frontal-subcortical neuronal circuits and clinical neuropsychiatry: an update. *J Psychosom Res* 2002;53:647–54.
37 Allman JM, Hakeem A, Erwin JM, *et al*. The anterior cingulate cortex. The evolution of an interface between emotion and cognition. *Ann N Y Acad Sci* 2001;935:107–17.
38 Devinsky O, Morrell MJ, Vogt BA. Contributions of anterior cingulate cortex to behavior. *Brain* 1995;118:279–306.
39 Mega MS, Cummings JL, Salloway S, *et al*. The limbic system: an anatomic, phylogenetic, and clinical perspective. *J Neuropsychiatry Clin Neurosci* 1997;9:315–30.
40 Waldemar G, Gauthier S, Jones R, *et al*. Effect of donepezil on emergence of apathy in mild to moderate Alzheimer's disease. *Int J Geriatr Psychiatry* 2011;26:150–7.